Geochemistry, Geophysics, Geosystems®

RESEARCH ARTICLE
10.1029/2022GC010576

Special Section:
Advances in understanding volcanic processes

Key Points:
- We detect multi-decade subsidence of up to 6 mm/yr across Timanfaya lavas emplaced almost 300 years ago using Interferometric Synthetic Aperture Radar time series
- Peak subsidence is consistent with the cooling of 100–150 m thick lava flows
- We demonstrate mitigation of time series bias from short-period interferograms in Sentinel-1 by using longer networks

Correspondence to:
V. Purcell,
ll15vr@leeds.ac.uk

Nearly Three Centuries of Lava Flow Subsidence at Timanfaya, Lanzarote

Victoria Purcell[1], Eoin Reddin[1], Susanna Ebmeier[1], Pablo J. González[2], Andrew Watson[1], Yu Morishita[3,4], and John Elliott[1]

[1]COMET, School of Earth and Environment, University of Leeds, Leeds, UK, [2]Department of Life and Earth Sciences (IPNA-CSIC), Consejo Superior de Investigaciones Cientificas, La Laguna, Spain, [3]Geography and Crustal Dynamics Research Center, Geospatial Information Authority of Japan, Tsukuba, Japan, [4]Now at Synspective, Tokyo, Japan

Abstract The 1730–1736 eruption on Lanzarote was one of the most significant volcanic eruptions to occur on the Canary Islands, with lavas covering over 200 km². Globally, it is volumetrically the third largest known subaerial basaltic fissure eruption in the past 1,100 years. Here we use Sentinel-1 and ENVISAT interferograms on both ascending and descending orbits to construct a time series of line-of-sight surface displacements and calculate linear vertical deformation rates. We resolve a constant subsidence rate of about 6 mm/yr associated with an area of ~20 km² within the central and western portion of the Timanfaya lava flows relative to the rest of the island. This is consistent over the 28-year period (1992–2020) covered by the Sentinel-1 and ENVISAT data when combined with the previously published European Remote-Sensing Satellite data. Time series constructed using Sentinel-1 short interval interferograms have previously been shown to suffer systematic biases and we find that by making longer period interferograms these biases can be mitigated (when compared against an averaged stack of 1-year interferograms). Cooling-driven contraction of an intrusion would require improbably large sill thickness to achieve the observed subsidence rates. Our observations are consistent with the cooling of lavas on the order of one hundred meters, twice as thick as previous estimates, which suggests overall lava volume for this eruption may have been underestimated. This is also evidence of the longest duration of lava flow subsidence ever imaged which indicates that these cumulative thick flows can continue to deform significantly even three centuries after emplacement.

Plain Language Summary A common result of a sustained volcanic eruption is large outpourings of lavas that can form thick flows when activity lasts many years. One of the ways to measure the behavior of active volcanoes is to use satellites to observe how fast parts of the volcano surface are moving. It is important to be able to estimate the different physical processes that may lead to the surface deformation around a volcano. One of these processes is the contraction of thick lava flows which rapidly subside due to cooling. Here we use radar satellites to measure how fast parts of Lanzarote are sinking. We find that despite these lava flows being nearly three centuries old, they are still sinking at about half a centimeter every year. These are the oldest flows known to still be measurably subsiding. This shows that when multiple stacked lava flows get very thick (here estimated at over 100 m in thickness), they are still able to continue deforming centuries later. It is important to know this is due to lava subsidence as other magmatic processes can also lead to subsidence and these might be of greater hazard concern and could indicate the subsurface migration of magma.

1. Introduction

Lanzarote is the northern and eastern-most Canary Island, located in the eastern Atlantic Ocean near the continental margin and about 100 km off the west coast of Africa (Figure 1a). Like the surrounding archipelago, it is a small volcanic intraplate oceanic island, mostly probably created over the last 15 million years from hot spot volcanism in the Miocene, Pliocene and the Quaternary (Carracedo et al., 1998; Hoernle & Schmincke, 1993). The long-term evolution of the islands, and the degree to which tectonic processes influence this, is still a matter of ongoing debate (Anguita & Hernán, 2000; Blanco-Montenegro et al., 2018; Negredo et al., 2022). The Lanzarote style of eruption activity is typified by low-explosive outpourings of basaltic magma from fissures (Carracedo et al., 1992). The largest of these events in the past half millennium was the 6-year intermittent eruption between 1730 and 1736, where an estimated 3–5 km³ (Carracedo, 2014) of material was erupted over much of the island of Lanzarote (Figure 1a). This eruption is also the third largest historical basaltic fissure eruption in the last 1,100 years behind a pair of Icelandic eruptions in 1783–84 Laki (Lakagígar), comprising 14 km³ of lava

Visualization: Victoria Purcell, Eoin Reddin, Susanna Ebmeier
Writing – original draft: Victoria Purcell, Eoin Reddin, Susanna Ebmeier, John Elliott
Writing – review & editing: Victoria Purcell, Eoin Reddin, Susanna Ebmeier, Pablo J. González, John Elliott

outpourings (Gudmundsson et al., 2008) from >100 vents along a 25 km long fissure (Thorarinsson, 1969) and the earlier 934–940 Eldgjá eruption of 20 km³ of lava along a 75 km long discontinuous fissure (Sigurardóttir et al., 2015). It is also similar in erupted volume to the largest known historical eruption in Africa at Dubbi volcano (Eritrea) estimated to be 3.5 km³ (Wiart & Oppenheimer, 2000). As way of modern comparison, the recent eruption at Kilauea in 2018 covered 35.5 km² with a volume of 0.8 km³ erupted from a 6.8 km long fissure (Neal et al., 2019), and the 2014–2015 basaltic fissure eruption at Holuhraun, Iceland, covered 84 km² with a volume of 1.44 km³ of lava (Pedersen et al., 2017). The 1730–1736 Lanzarote erupted volume was 15–26 times larger than the estimated extruded volume of almost 0.19 km³ from the 2021 flank eruption of Cumbre Vieja at La Palma in the western Canaries (Carracedo et al., 2022; González, 2022), which lasted almost 3 months covering an area of 12 km² in lava flows over 50 m thick in places.

The period of major activity on Lanzarote initiated on the 1 September 1730 with a large earth tremor and continued in a number of punctuated phases at varying eruptive centers until ceasing on the 16 April 1736 (Romero et al., 2019), spanning a total period of 2055 days of discontinuous volcanism. Activity is recognized as being broken up into five major phases across almost 6 years of eruption (Carracedo et al., 1992). Initially the lavas predominately flowed out to the north-west, then to the west and west-south-west and again back to the north-west in the latter phases. The erupted material was emplaced mainly as 'a'ā and pāhoehoe lava flows, covering an area greater than 200 km² (Solana et al., 2004a), equivalent to a quarter of the current island (810 km²), erupting from an east-west trending fissure about 15 km long and comprising multiple volcanic vents (Figure 1b). Over the course of the multiple eruptions that produced the Timanfaya volcanic field, 30 volcanic cones of varying morphology of cinder, slag and spatter formed (Romero et al., 2019). One of these volcanic vents is Timanfaya, which was created during the fourth, highly effusive phase. The lava from this phase of the eruption flowed from Timanfaya and the surrounding cones North-Westwards to the coast (Carracedo et al., 1992).

Thicknesses of these emplaced flows have been estimated to be between a few meters and 60 m (Araña et al., 1973; Sharma, 2005). However, these estimates carry significant uncertainties, as there are few places where the flow depth is exposed and can be measured directly, but coastal exposures of lava flows in the west are observed as thick as 30–50 m (Sharma, 2005). The current topography of Lanzarote (Figure 1b) reflects the previous volcanic activity of the island with dozens of cones being constructed in the various volcanic phases. There are two chains of cinder cones clearly visible in the digital elevation model (DEM) of the area (Figure 1b). The first is associated with the 1730–1736 eruption with an ENE-WSW orientation of cone alignment. The second chain, to the south of the 1730–1736 lava flows is linked with historic island building events. Since the end of the main eruptive phase in 1736, there has only been one other volcanic eruption in 1824. The 1824 eruption was much shorter in duration (two and a half months) and far smaller in erupted volume, with the resulting lava flows emplaced on top of the 1730–1736 flows to the north (flowing northwards down to the coast) and north-east of Timanfaya (Figure 1a) at two isolated cones and a third further to the east-north-east outside Timanfaya (Romero et al., 2019).

Present-day activity is limited to anomalous high heat flow, distributed over topographic highs in a 20 km² area around Timanfaya (Figure 1). In the 1970s, a hundred thermometers buried at 3 m on Lanzarote measured temperatures up to 350°C and in deeper wells at 150–250 m, thermal gradients of 0.2°C/m were found (Araña et al., 1973). Islote de Hilario, site of the national park visitor center (Figure 1c), has the highest temperature anomalies, with Araña et al. (1984) reporting a maximum temperature of 380°C at 6–9 m depth and 605°C at 13 m depth. A magnetotelluric study of Timanfaya detected a highly conductive subsurface body which was interpreted as a magma chamber at 4 km depth with temperatures >900°C associated with the 1730–1736 eruption (Ortiz et al., 1986). From almost 300 gravity station measurements across Lanzarote, Camacho et al. (2001) obtained a 3-D density contrast model of upper crustal anomalies and found shallow density lows with ENE-WSW and WNW-ESE alignments beneath Timanfaya that may be associated with the recent volcanism. However, a spatially denser gravity survey and crust density inversion model points to a lack of observable magma chamber beneath Timanfaya (Camacho et al., 2019).

Interferometric Synthetic Aperture Radar (InSAR) is a remote sensing technique used to show deformation over a certain time period by differencing two SAR images of the same area acquired at different times (Goldstein & Werner, 1998). Observations using InSAR are now used for volcanic monitoring in many parts of the world, primarily focused on deformation caused by current volcanic or magmatic activity. However, InSAR measurements have also captured remnant deformation from historical eruptions or intrusions (Chaussard, 2016; Ebmeier, 2016; Parker et al., 2014; Wittmann et al., 2017). A measurable subsidence signal caused by volcanic
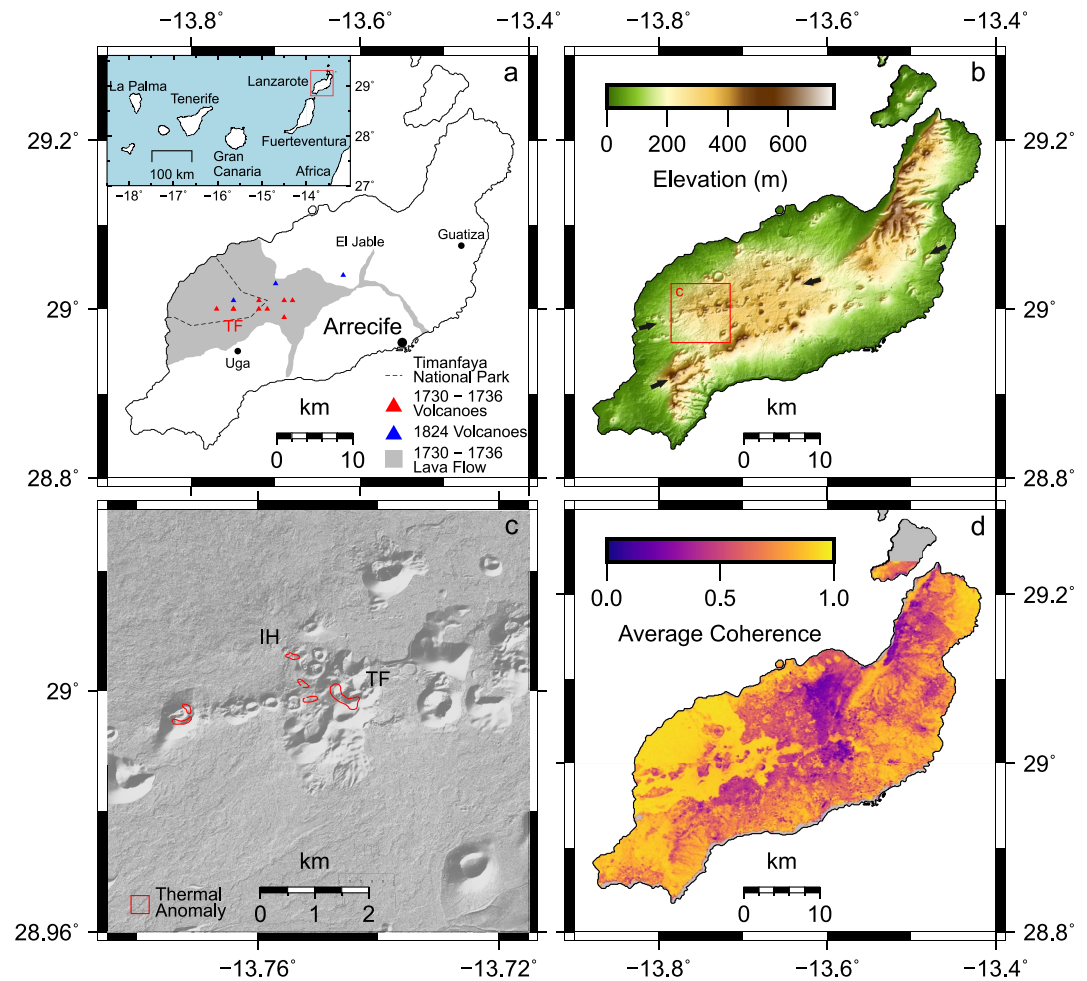
Figure 1. (a) Distribution of ~200 km² of emplaced lava flows from the 1730–1736 eruption on Lanzarote (Carracedo et al., 1992), with the major eruptive centers indicated (red triangles), which are predominately within the designated area of the Timanfaya National Park (TNP). TF—Timanfaya. The blue triangles indicate the cinder cones associated with the 1824 eruption. The insert shows the relative position of Lanzarote to the other Canary Islands in the Eastern Atlantic Ocean and the African coastline. (b) Down-sampled LiDAR digital elevation model (DEM) of Lanzarote at 10 m resolution of the entire island topography. The black arrows show the two chains of cinder cones on the island referred to in the text. (c) Sub meter LiDAR DEM from 2015 of Timanfaya area (Spanish National Geographic Information Center). The locations of previously measured thermal anomalies (Araña et al., 1984) are indicated by red outlines with the northern most one associated with the national park visitor center at Islote de Hilario (IH). (d) Average mean Interferometric Synthetic Aperture Radar coherence from the descending Sentinel-1 interferograms highlighting the stable lava flows with high coherence (yellow) and low coherence in the more mobile sandy regions of the island center (El Jable). Note the magnitude and pattern of coherence is similar for the ascending track.

activity centuries after it took place, has implications for future volcanic monitoring in regions of long-term effusive activity, especially where background historic subsidence rates need be removed to isolate any new magma movement (Stevens et al., 2001).

InSAR measurements have previously been used to measure decadal timescale surface deformation rates across the island of Lanzarote. González and Fernández (2011) used synthetic aperture radar data from European Remote-Sensing Satellite (ERS)-1/2 for the period 1992–2000 and found an area centered on the thermal anomalies near Islote de Hilario (Figure 1c) to be subsiding about 4–6 mm/yr whilst the rest of the island was largely stable (at the 1 mm/yr noise level). Given the spatial overlap of the deformation area with the surface temperature highs and previous geophysical data and models, their preferred hypothesis was that magma crystallization from cooling and contraction of a shallow magmatic body beneath Timanfaya was still ongoing. We used the results they present for deformation rates during the nineties to extend our time series back in time by combining their

observations with ours from more recent SAR satellites of ENVISAT (2004–2010) and Sentinel-1 (2016–2020). Other sources of surface displacement observations come from Global Navigation Satellite System (GNSS) data such as from Riccardi et al. (2018) who measured deformation rates for 3 years from five permanent GNSS sites across the island finding a maximum subsidence rate of 6.1 ± 1.7 mm/yr at the location of the thermal anomalies within the Timanfaya National Park (TNP), with most of the other vertical rates at sites across the island outside of Timanfaya stable within uncertainty.

The millimeter per year rates of subsidence expected here and previously measured for Lanzarote (González & Fernández, 2011) are comparable to the detection limit for InSAR time series analysis for volcanic processes (Ebmeier et al., 2013) given the anticipated noise from the differential atmosphere delay, which is expected to be particularly large for an oceanic island environment (Webb et al., 2020). To reduce the impact from tropospheric water vapor we tested using both an external weather model for atmospheric correction of phase delay and also an empirical linear correction of measured phase with topography within the individual interferograms. We also performed Independent Component Analysis (ICA) (Ebmeier, 2016) to extract the signal of subsidence and separate it from contributions of atmospheric noise over the Timanfaya National Park area. This latter approach is performed to yield a slightly cleaner signal, and to assess whether the two regions of subsidence centered on Timanfaya and along the north-west coast are within the same extracted independent component.

Additionally, interferometric use of Sentinel-1 data has been shown to suffer systematic phase biases (De Zan et al., 2015), often termed a fading signal, due to use of short interval interferograms in time series analysis, which results in an apparent relative subsidence of many land surfaces in the derived velocity fields. As our aim here is to assess the temporal and spatial extent of subsidence patterns associated with volcanic processes, it is important to account for sources of contamination from such phase bias due to our choice of network design. To test the phase bias contribution of the shorter interval interferograms, we used a range of short (half a month) and longer (up to a couple of months) temporal baseline networks and compare the resulting derived velocities with each other as well as with an averaged stack of independent 1 year interferograms. Our aim was to find if the phase bias is generally present across much of the island, and whether there are significant areas with greater biases that might be associated with vegetation outside of the Timanfaya region (which itself is almost entirely devoid of vegetation and thus might be expected to not be affected). We made longer period interferograms as a reference data set against which to compare the change in amount of bias in different network lengths (i.e., when compared against an averaged stack of independent 1-year interferograms).

In this study, we performed InSAR time series analysis and combined three decades of surface deformation data to derive vertical rates of motion across the island of Lanzarote. We tested corrections to mitigate the atmospheric noise in the interferograms and also examined the systematic bias due to the use of time series networks of different interferogram length. We ruled out cooling-driven contraction of a sill as the origin of the subsidence by comparing the predictions of crystallisation models to our measurements. We then made estimates of the minimum lava flow thicknesses required for the contemporary subsidence to be due to thermal contraction of the Timanfaya lava flows. We discuss the implications for the volume estimates if the cooling lava model is correct, which suggests flows of 100+ m thickness, indicating erupted lava volumes larger than previously estimated.

2. Data and Methods

2.1. InSAR Processing and Time Series Analysis

We used time series analysis of over 4000 interferograms from Sentinel-1 and ENVISAT (Table 1) to give line-of-sight deformation rates. We used both descending and ascending images to decompose the deformation rates into vertical and East-West velocities. The different data sets were tied to a common spatial reference area by removing the mean rate of the regions of the island not affected by the 1700's volcanism (Figure 1a). When combined with previous published ERS results for the period 1992–2000 (González & Fernández, 2011), this yields a velocity time series covering most of the past 28 years from 1992 to 2020.

European Remote-Sensing Satellite and ENVISAT data were processed following the methodology presented by González and Fernández (2011). We coregistered all scenes to a common reference primary date geometry for each orbital pass (ascending and descending), and computed differential interferograms using the DORIS software (Kampes et al., 2004). Topographic contributions were removed using the 3-arcsec Shuttle Radar Topography Mission DEM, at a spatial multilooking factor for the SAR of 4 looks in range and 20 looks in azimuth

Table 1
Key Parameters of ERS (González & Fernández, 2011), ENVISAT and Sentinel-1 Data Sets (This Study) for the Two Acquisition Directions of Ascending (Asc) and Descending (Dsc)

	ERS-1/2	ENVISAT		Sentinel-1A/B	
Satellite	Dsc	Asc	Dsc	Asc	Dsc
Track no.	266	302	266	089	023
Time Period Covered	1992/09/02 – 2000/01/08	2006/02/27 – 2010/06/21	2004/01/17 – 2010/01/30	2017/01/10 – 2020/06/29	2016/09/14 – 2020/06/25
Epochs	14	34	21	200	207
Interferograms	91	105	86	2134	2211

Note. Dates are given in the format YYYY/MM/DD. The number of interferograms for the Sentinel-1 datasets represents the maximum analyzed and is the total using the full 11 forward connections between epochs. ERS, European Remote-Sensing Satellite.

(80×80 m pixel area). A subset of pixels were selected based on the average spatial coherence greater than 0.25. Time series of displacements were obtained for this subset of pixels, inverting the interferograms unwrapped phases. The unwrapping was completed with SNAPHU (Chen & Zebker, 2000).

The Sentinel-1 interferograms were made using the commercial software GAMMA (Werner et al., 2000, version 20181130) and the time series analysis (Figure A1) was completed using the openly available software code LiCSBAS (Morishita et al., 2020), using a small baseline approach (Berardino et al., 2002) of connected interferogram networks.

We processed a combined total of 407 Interferometric Wide Swath (IWS) images from Sentinel-1A/B (Torres et al., 2012) from one ascending (089) and one descending (023) track (Table 1) with common spatial coverage of almost the entire main island of Lanzarote ($\sim$800 km^2). The time period covered by the acquisitions is from late 2016/beginning of 2017 when systematic coverage over the area started from Sentinel-1 and for this study is complete up until mid 2020 (Figure A2). During this period, Sentinel-1B acquired on every ascending and descending pass (every 12 days). From May 2017 Sentinel-1A also started acquiring over the area (and on each pass), giving a combined 6-day repeat interval for most of the time series (the shortest achievable with the 2-satellite Sentinel-1 constellation).

Sentinel-1 IWS data was acquired in Terrain Observation with Progressive Scans (TOPS) mode (Yagüe-Martínez et al., 2016) on three subswaths in bursts of $\sim$20 km in length in the along-track azimuth direction. We processed the data from Level-1 Single Look Complex (SLC) images and extracted the three consecutive bursts on the central subswath 2 for both descending and ascending tracks to give almost complete coverage of the main island ($\sim$800 km^2) and used the precise orbital ephemerides data from the European Space Agency (ESA). We initially resampled the SLCs to a reference primary date using a cross-correlation method and then refined this to the high precision required for TOPS mode acquisitions using the Spectral Diversity method (Yagüe-Martínez et al., 2016). Further details are provided by Lazecký et al. (2020).

We formed differential multi-looked interferograms between successive acquisition dates (epochs) with 10 looks in range and 2 in azimuth to give pixels of approximately 30 m ground spacing. For the purpose of analysis of the phase bias problem we generated two different sets of independent interferograms but across the same period of time (2017–2020). First we generated a connected network of interferograms between each epoch and the next 11 closest epochs (creating interferograms typically spanning from 6 days up to 2 months interval) which we later sub-sampled to create shorter period networks for comparisons. Second we generated a set of independent interferograms of 1 year in length by connecting each epoch only once to an epoch $\sim$365 days ahead. We used the 1 arc-second Shuttle Radar Topography Mission (SRTM) (Farr et al., 2007) to remove the contributions to the phase from topography and for geocoding the results. We spatially filtered the data using an adaptive power spectrum approach (Goldstein & Werner, 1998) with a filtering window size of 64 pixels and a filtering exponent of 0.3 and then unwrapped the data in areas with a coherence above 0.1 using a minimum cost function algorithm (Wegmüller et al., 2002) to give a line-of-site displacement for each interferogram.

In order to calculate the average displacement rates from the stack of data as a reference data set, we simply summed all the independent 1-year interferograms and divide by the number of observations (144 in descending and 138 in ascending) to yield an average velocity (Figure 2).

For the time series analysis using the connected network of interferograms in a small baseline subset (SBAS) approach we used the LiCSBAS open-source package to generate surface velocities (Morishita, 2021; Morishita et al., 2020). LiCSBAS performs a number of masking, quality and loop closure checks to identify bad interferograms and pixels before performing a small baseline inversion. The mask and filter thresholds we used (Table A1) were mostly the default parameters provided within LiCSBAS. A coherence value of 0.25 was chosen as this is the same mask threshold applied to the ERS and ENVISAT data. The number of permissible loop errors was also reduced to 1. The minimum height used in the linear elevation-phase correction was reduced to 0 m, as much of Lanzarote's topography is under the default value of 200 m (Figure 1b), the highest elevation of the island being 671 m. For the final filtering of the time series, we first subtracted a linear ramp from each interferogram in our network, before a Gaussian spatio-temporal filter that is a one dimensional high pass filter in time and two dimensional low-pass in space is applied with a temporal width of 20 days and a spatial width of 2 km respectively. Standard deviations were calculated for the velocities by using a bootstrap method to randomly resample the data set with data replacement 100 times, computing velocities for each iteration. See Morishita et al. (2020) for more details.

To spatially co-reference the ERS, ENVISAT and Sentinel data we removed the mean of a selected area of stable pixels, after applying a single mask. The mask was created by removing any pixel with a clear and obvious deformation or noise signal in any of the velocity images from visual inspection of the average velocity maps. GNSS spatial referencing was explored, but Lanzarote has five permanent GNSS stations. Two of these (LZ01 and LZ02) were only installed in late 2018 and therefore there is not enough data to be reliably used for referencing. HIRA is also located at 29.15°N, 13.49°E, which is masked due to poor coherence in datasets, except in the ascending ENVISAT. We decided that the two remaining GNSS stations were not sufficient for referencing the InSAR velocities, but we used these later for comparison with our data (Figure A3). GNSS data were downloaded from the Nevada Geodetic Laboratory (Blewitt et al., 2018).

2.2. Phase Bias

Systematic phase bias (De Zan et al., 2015) that affects velocity estimates in InSAR times series has a major impact on accurately estimating small rates of surface deformation. These fading signals have been attributed to the result of soil moisture (De Zan & Gomba, 2018) that causes a breakdown in the phase consistency in triplets of interferograms (De Zan et al., 2014) which occurs as a result of the multi-looking and spatial filtering that is commonly implemented in interferogram processing strategies (Michaelides et al., 2019). It particularly affects short period interferograms (Ansari et al., 2021; Maghsoudi et al., 2022) of weeks to a few months, and whilst in any individual interferogram the error is small compared to other noise terms such as from the atmosphere, cumulatively it propagates from the network time series causing a systematic bias error that varies spatially. This bias affects both look directions in a similar fashion (usually a negative bias). Therefore, when the two look directions are combined to decompose the line-of-sight displacements into vertical and east-west, the negative bias reinforces for up-down motion but largely cancels for horizontal estimates. As a result the bias creates erroneous regions of apparent subsidence whereas horizontal measurements will be less biased by this effect.

We explored the phase bias contribution from the Sentinel-1 data by varying the number of interferograms made from each epoch in the network used for the velocity inversion. We compared the resulting estimates of deformation rates with each other, and with land cover. The greater the number of connections created, the longer the average interferogram length and the denser the network (Figure A2). However, this comes at the expense of processing time and loss of coherence in the longer period interferograms, reducing spatial coverage, such as in the sandier areas in the center of the island (El Jable).

We found that the estimated surface velocity varies markedly across the island depending on how the network of interferograms is constructed (Figure 2), even though all the same observation epochs are used in each case. By increasing the number of forward connections when forming interferograms in the network from 3 (Figures 2a and 2b) to 11 (Figures 2c and 2d), the apparent negative line-of-sight velocities across many parts of the island in both ascending and descending are reduced. Additionally, regions of apparent positive velocities in the center
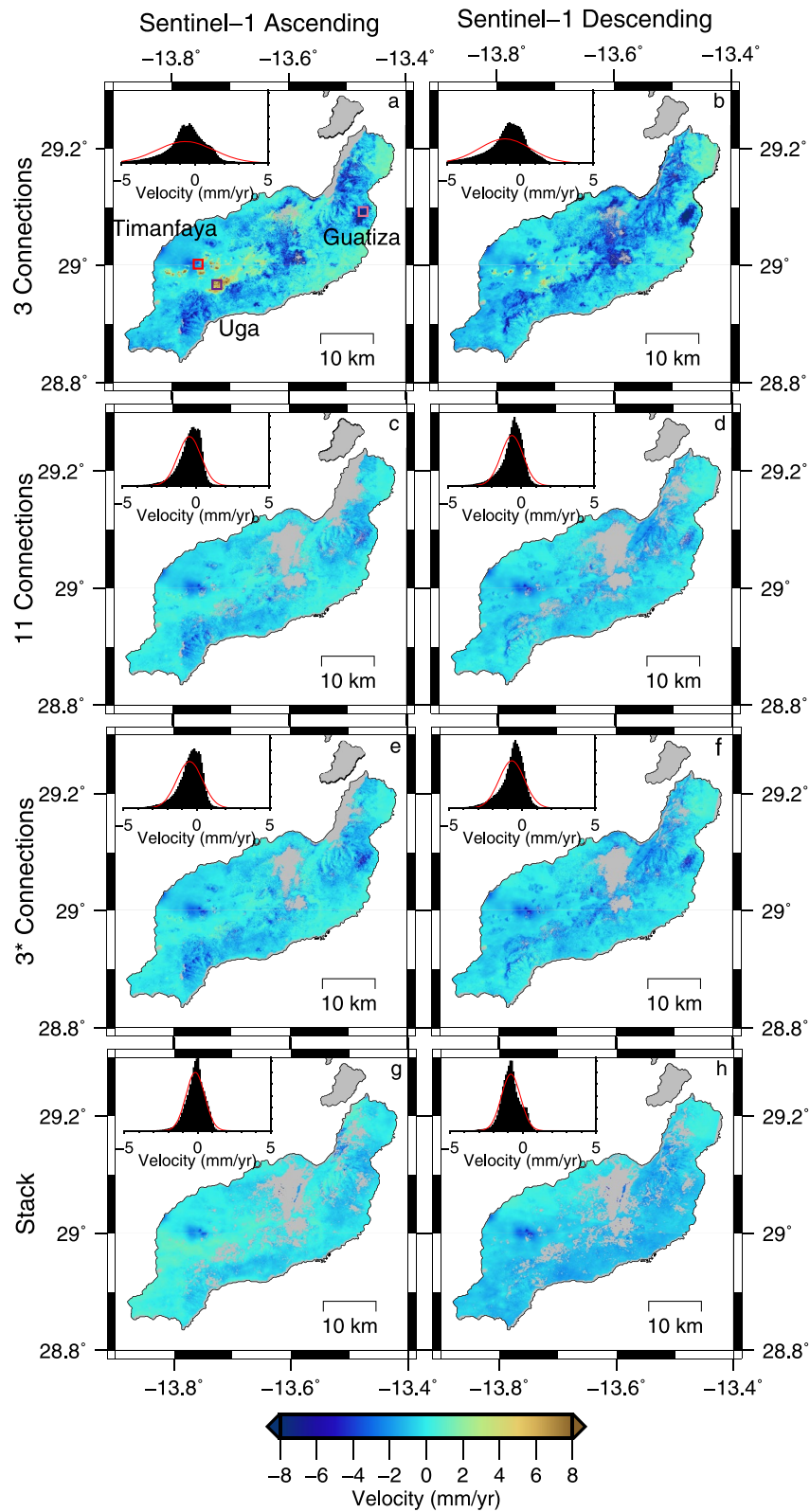
Figure 2.

Table 2
Mean Interferogram Length, Mean Velocity and Standard Deviation of Each Velocity Map Across the Whole Island Created by Varying the Number of Interferogram Connections in Creating the Network Used for the Velocity Inversion

		No. of connections						
		3	5	7	9	11	3*	Stack
Ascending	Mean Interferogram Length (days)	12.7	18.9	25.1	31.2	37.3	37.7	365.8
	Mean Velocity (mm/yr)	−0.65	−0.51	−0.49	−0.47	−0.43	−0.48	−0.15
	Standard Deviation (mm/yr)	1.94	1.30	1.01	0.87	0.79	0.88	0.64
Descending	Mean Interferogram Length (days)	13.3	19.9	26.4	32.9	39.3	39.7	365.9
	Mean Velocity (mm/yr)	−1.06	−0.86	−0.76	−0.69	−0.63	−0.70	−0.82
	Standard Deviation (mm/yr)	1.74	1.20	0.96	0.84	0.76	0.86	0.65

of the island observed in the shortest interferogram network disappeared in the longer networks. The spread in velocity also became more Gaussian in distribution with increasing network length, with reduced noise as seen by the smaller standard deviation for both ascending and descending look directions (Figure 2).

We tested the impact of interferogram duration on velocity estimates, as opposed to the number of interferograms in the network, by creating a second network consisting of 3 longer timespan forward connections (interferograms) from each epoch (Figures 2e and 2f and Table 2). We selected a connected network of interferograms to proceed to time series processing to check the phase closure loops (Figure A2), which results in an average interferogram length of 38–40 days. Such a network design achieved similar results to that made with 9 connections (Figure A4 and Table 2), but significantly reduced the processing time as only one third of the number of interferograms were required.

Since the Sentinel-1 coherence of Lanzarote is excellent (Figure 1d), we were also able to create a stacked velocity map made by averaging all possible independent 1-year long interferograms (144 for descending and 138 for ascending) as a reference data set for comparison that we would expect to not be affected by any systematic phase bias. These velocities had lower standard deviations (0.65 mm/yr) in both the ascending and descending look directions than those derived from time series analysis.

Phase bias signals in our shorter-interferogram networks are correlated with land cover, especially agriculture and viticulture. There were significant areas of apparent subsidence immediately north of the village of Guatiza in the north-east of the island where there is extensive agriculture. This apparent subsidence also occurred in the region running along the older chain of cinder cones through the central spine of Lanzarote (Figures 2a and 2b). These negative velocities gradually reduce as the number of connections is increased (Figures 2c and 2d). Likewise, the apparent uplift near the village of Uga (on the southern edge of Timanfaya) seen in shorter networks (Figure 3b) reduced to almost 0 mm/yr after employing seven or more connections. In contrast, the average subsidence signal near Timanfaya remained approximately constant (Figure 3a) with increasing network length, but the extent of the signal became more evident in the longer networks as the spurious positive signals to the south were attenuated. The coefficient of determination R^2 values for the relationship between the velocity and the average interferogram network length (Table 2) show that there is little to no correlation in the variation at Timanfaya. The R^2 values are significantly higher for Uga and Guatiza indicating a strong dependence on the retrieved estimate and the length of network employed for these areas. However we note that the number of masked pixels varies between the different networks. At Timanfaya the percentage of masked pixels is less than 4% for all networks in both the ascending and descending datasets. This is because the lava flows coherence remains high even in the longest interferograms. At Uga for the ascending orbit the percentage of masked pixels is 0.5% and 40% for the 3 and 11 network respectively. In the descending orbit these percentages are 1% and 66%. At Guatiza for the

Figure 2. Sentinel-1 average line-of-sight velocity maps constructed from varying the number of network interferogram connections used in the time series inversion. The number of connections refers to the number of interferograms made from each epoch forward in time (networks are shown in Figure A2. The 3 and 11 connection networks were made with the shortest possible interval interferograms. The 3* network had the same number of interferograms as in the ordinary 3 connection network but with a longer average interferogram length (Table 2). The final stack version was made by averaging all independent ~1 year interferograms. Inset histograms in each panel show the distribution of the velocities and a normal distribution fit (red line).
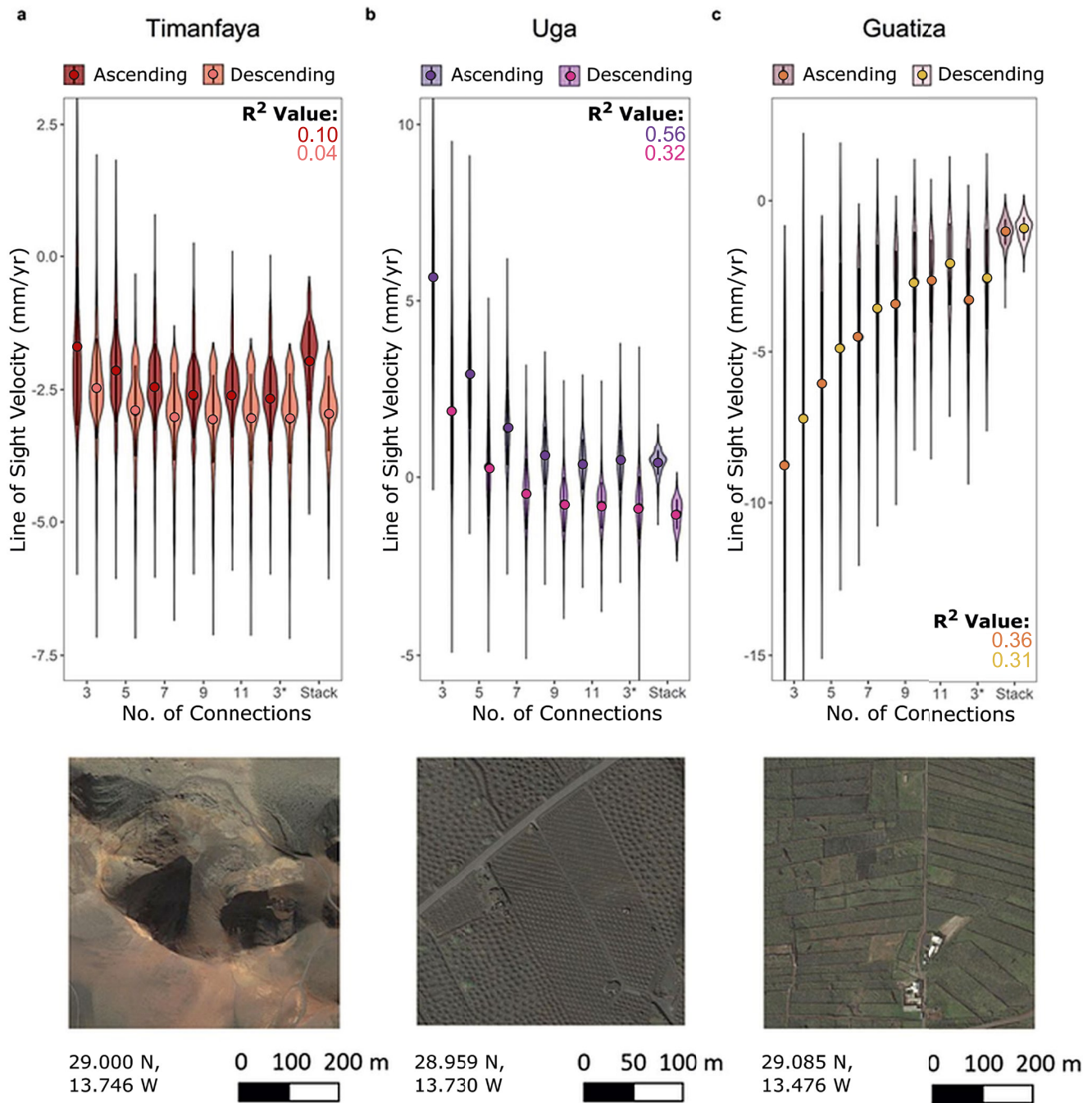
Figure 3. Violin plots showing the distribution of velocities for each network at Timanfaya, Uga and Guatiza (optical satellite image and location of each region in lower panels). The colored dot of each violin indicates the mean value, with the line showing one standard deviation. The R^2 values are also given for the variation in velocity compared to the variation in average interferogram network length (excluding the stack value). Note there are a variable number of pixels for each plot as coherence typically reduces for larger network connections with longer interferograms.

ascending orbit the percentage of masked pixels is 0.1% and 23% for the 3 and 11 network respectively. In the descending orbit these percentages are 0.3% and 23%.

Visual inspection of optical satellite imagery of Lanzarote showed that the land surface just north of Guatiza (Figure 3) is covered by cultivated fields. A possible source of localized subsidence in agricultural regions might be groundwater extraction. However, information from the current and most recent Lanzarote hydrological plan indicates that no water for irrigation is directly pumped out from groundwater resources in this location

(www.aguaslanzarote.com). Therefore, we speculated that the negative phase bias seen here is associated with the variation in soil moisture over time caused by rainfall and the asymmetrical wetting and drying of the land (De Zan & Gomba, 2018). For this area the difference between the 3 and 11 network average velocities was 6.2 mm/yr in the ascending and 5.1 mm/yr in the descending. This is comparable with corrections of up to 27.4 mm/yr in cropland areas in Turkey, attributed to phase bias (Maghsoudi et al., 2022).

To the north-east of the village of Uga (Figure 3) there are over a hundred thousand artificially constructed hollows, typically ~10 m in diameter, spread across 10 km². These circular depressions are designed to capture and retain moisture for viticulture through the application of the porous scoria on top of the soils, which traps moisture from the overnight humidity close to the ground (dew), making agriculture possible in otherwise dry and windy conditions. These cultivated regions resulted in a particularly strong positive phase bias that disappeared with longer period interferogram connections. The bias effect was stronger in the ascending pass (early evening) for shorter connections which indicates an impact of the time of day on the degree of bias for these types of land cover.

The Timanfaya lava flows have not yet developed soil cover, and the bare rock appears not to generate phase biases: velocities are relatively consistent, irrespective of network design (Figure 3).

Our analysis showed that choice of interferogram duration has a large impact on the retrieval of surface displacements at rates below a centimeter per year. We demonstrated that this phase bias can be mitigated with a network of longer period interferograms. For our data, networks with interferograms averaging more than 30 days in time span begin to more closely approximate velocities derived from stacks of 1 year interferograms.

For our subsequent time series analysis, we proceeded using the 11 connection Sentinel-1 data set, but we note that an acceptable trade-off between limiting the phase bias and processing time could also be achieved by making a smaller subset of the longer interferograms (Figures 2 and 3).

2.3. Atmospheric Corrections

Variations in the water vapor content of the troposphere lead to changes in refractivity and subsequent path length differences for microwaves such as from repeat-pass SAR. Such fluctuations are one of the largest sources of noise in InSAR analysis as differences in the state of the atmosphere between acquisitions can result in differential path delays a couple of orders of magnitude greater than some of the smallest surface deformation signals of interest. Various methods have been employed to try to mitigate such atmospheric contamination (Li et al., 2019), and here we used empirical linear atmospheric corrections applied to the ERS, ENVISAT and Sentinel-1 interferograms (Morishita et al., 2020). Additionally, we also tested the tropospheric delay estimates from the Generic Atmospheric Correction Online Service for InSAR (GACOS) (C. Yu, Li, Penna, & Crippa, 2018) applied to the sets of Sentinel-1 interferograms (Figure 4) to assess its relative performance over this ocean island.

The topographically correlated component of atmospheric noise was estimated using the linear phase elevation correction implemented in the final step of time series analysis performed in LiCSBAS (Morishita et al., 2020), with the default elevation mask lowered from 200 to 0 m here to account for the low-lying topography of the island. As it is an empirical method, it necessarily reduced (or at the very least leaves approximately the same) each of the interferograms (Figure 5) in terms of the standard deviation in the line-of-sight displacement across the island. For the ascending passes (which are acquired early evening, 18:57 UTC) there are some large reductions in the standard deviation of some interferograms, which is observed to a lesser extent for the descending (early morning 06:54 UTC) passes. However, in terms of the final average velocity derived from the time series analysis (Figure 4), the difference between the original non-corrected velocity maps and the linear corrected ones is small (Figure A5), with a maximum residual of 0.8 mm/yr in the ascending and 1.2 mm/yr in the descending. This modest change is likely because of the low elevation relief (Figure 1b) of much the island, resulting in a limited phase-elevation dependence in terms of a stratified troposphere water vapor (or at least a lack of consistent linear relationship across both sides of the island).

The Generic Atmospheric Correction Online Service for InSAR (GACOS) provides zenith total delay maps for correcting atmospheric noise in SAR interferograms using high resolution weather model data from the European Centre for Medium-Range Weather Forecasts (C. Yu, Li, & Penna, 2018; C. Yu, Li, Penna, & Crippa, 2018). The use of this correction can be applied in the initial steps of the LiCSBAS processing chain where the zenith
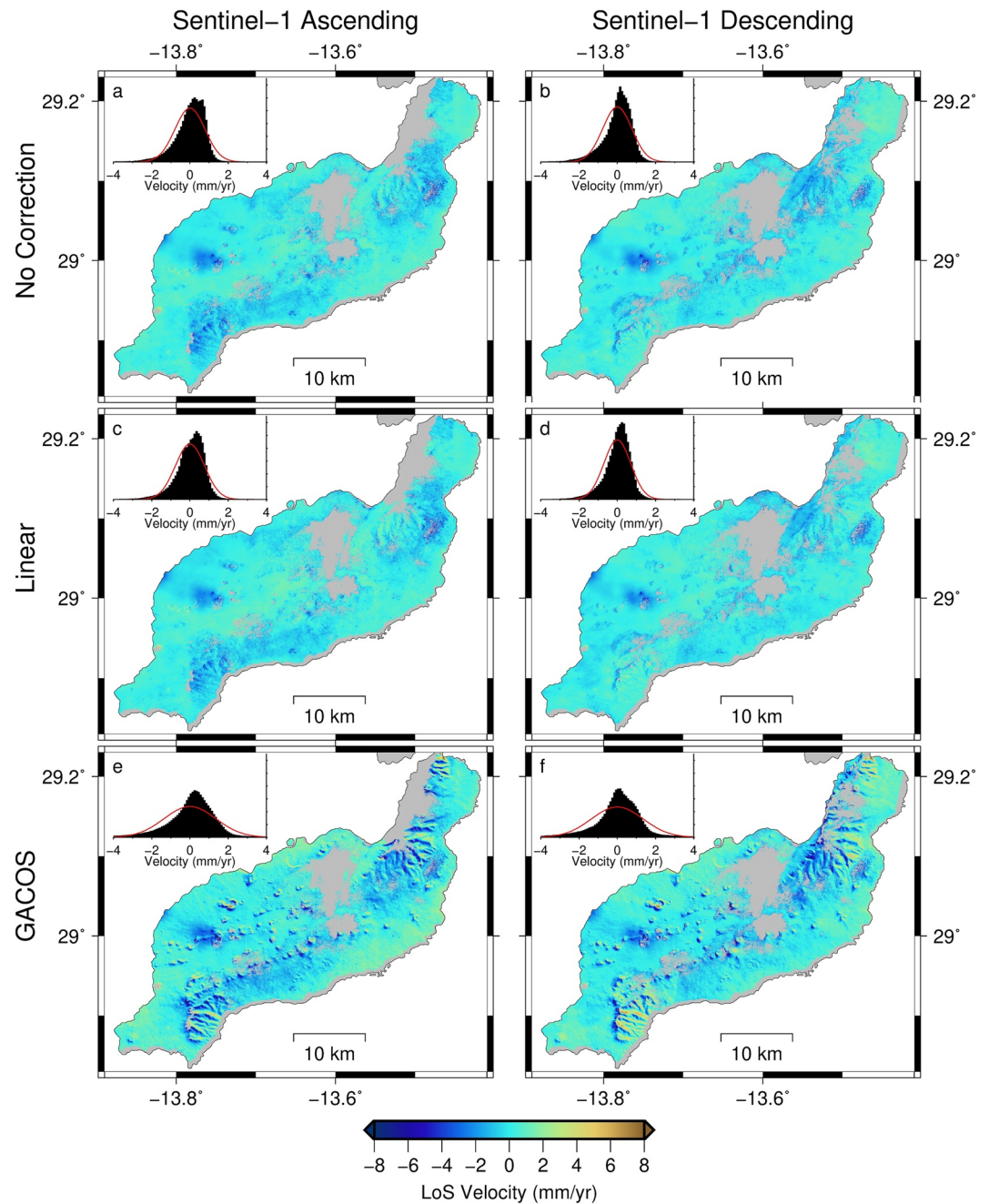
Figure 4. Sentinel-1 line-of-sight velocities from the 11 connected network with no atmospheric correction applied for ascending and descending look directions (a, b), an empirical linear phase versus elevation correction based upon the signal correlation with height implemented in LiCSBAS (c, d) and an atmospheric weather model correction from Generic Atmospheric Correction Online Service applied prior to the time series estimation (e, f).

total delays for each epoch are converted into a differential line-of-sight path delay for each interferogram. The GACOS correction improved 45% of the interferograms in terms of the standard deviation of phase across the whole island for the 4223 interferograms but the overall average standard deviation was degraded by 7.0% for the descending interferograms and 7.2% for the ascending (Figure 5). GACOS is not optimized for correcting atmospheric delay on small ocean islands, due to the low spatial resolution of the ECMWF model used and the 6-hr temporal resolution. At its widest points, Lanzarote is only 35 km in extent from East to West and 25 km North to South. The resolution of the ECMWF weather model used in GACOS is about ~10 km (0.125° degree spacing).
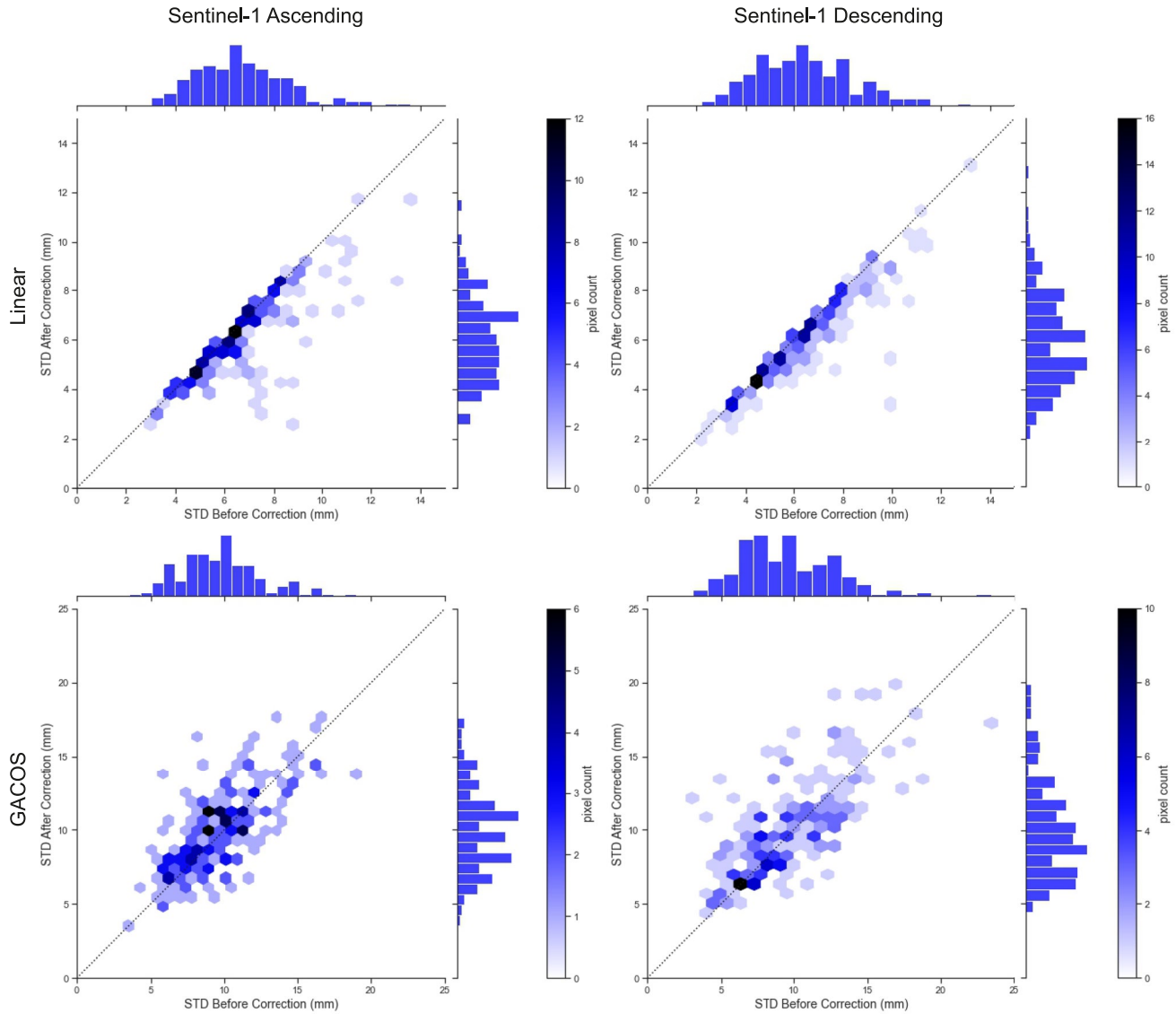
Figure 5. Comparison of the standard deviations of the Sentinel-1 displacement for the shortest interferograms from every epoch before and after each atmospheric correction. The color of the pixel indicates the frequency of interferograms represented by that point. Points below the line of equity represent an improvement in the standard deviation after the correction. The difference in range of standard deviations before the correction between the linear and Generic Atmospheric Correction Online Service correction reflects the place within the LiCSBAS processing that each correction occurs.

Therefore, the introduction of noise from the GACOS correction may be as a result of a mistiming in models of the actual passage of weather fronts (Wadge et al., 2010) passing over the island and the inability to capture the short-wavelength spatial turbulence (Cao et al., 2021). The increase in the standard deviation is particularly greater for the early evening ascending pass which may be because the more turbulent atmosphere at the end of the day is not captured by models.

We therefore used only the linear phase-elevation corrected interferograms for the 11 connection network in our time series analysis. Comparing the maps of the Sentinel-1 average line-of-sight velocities on respective look directions with those from ENVISAT, we see very good agreement in both the spatial patterns and magnitude of the signal over Timanfaya (Figure 6). Similarly, both descending passes from ENVISAT and Sentinel match the velocities in the previously published ERS data from González & Fernández (2011). The standard deviations for the line-of-sight velocities can be found in the Appendix (Figure A6).
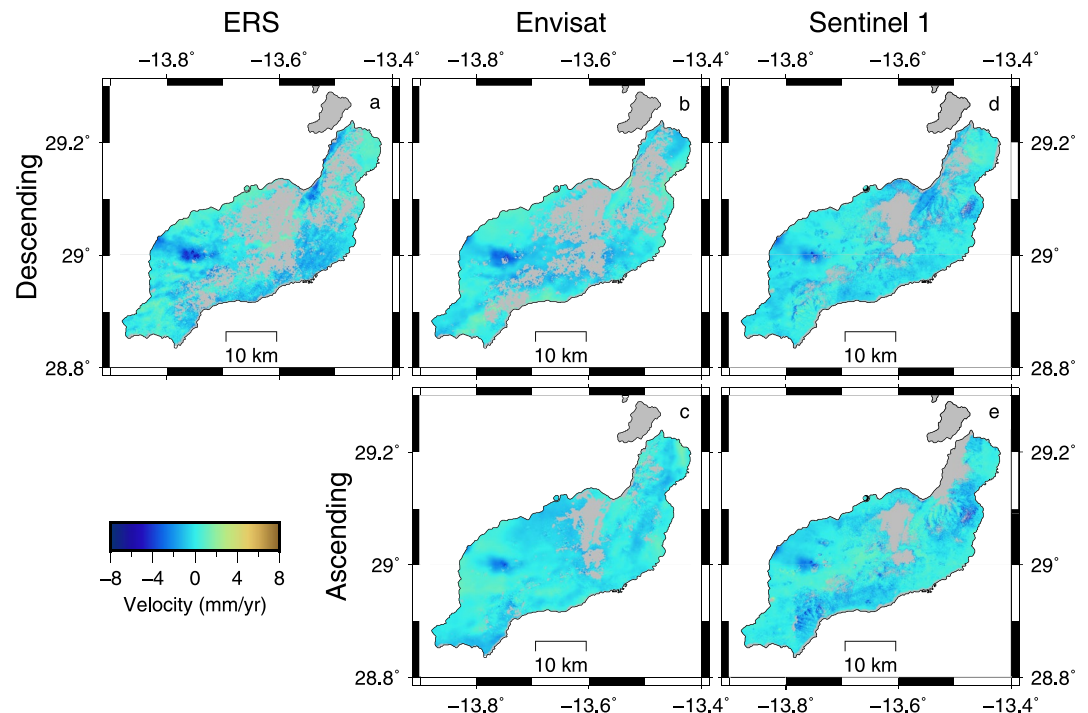
Figure 6. Comparison of the Interferometric Synthetic Aperture Radar derived line-of-sight velocities for the whole island from (a) previously published results with European Remote-Sensing Satellite (ERS; González & Fernández, 2011) and from the analysis here of (b, c) ENVISAT and (d, e) Sentinel-1 on both look directions.

2.4. Vertical Deformation

We combined the ascending and descending average line-of-sight rates (for ENVISAT and Sentinel-1) to resolve the velocities into two components of vertical and east-west motion on a pixel-by-pixel basis (Figures 7 and A7). Using the method set out by X. Yu et al. (2017) we assumed the north-south component was negligible. As the two line-of-sight look directions are much less sensitive to north-south motion, deviations from this assumption would have minimal impact on the accuracy of the retrieval of the other two components.

The decomposition was performed on both the Sentinel-1 and ENVISAT velocities, whilst for comparison with the ERS data with only one look direction on the descending track, we further assume that all of the ERS line-of-sight represents vertical motion and resolve that component into this direction based upon the angle of incidence. This is supported by the retrieved Sentinel-1 east-west velocities (Figure A7) which show that there is little to no relative horizontal movement across the whole island. The ENVISAT east-west results are noisier than Sentinel-1, but in the Timanfaya National Park area, the range is small, between −1 and 1 mm/yr. The lack of horizontal movement across the deforming region points more to a vertical dominated process.

2.5. Independent Component Analysis

We used Independent Component Analysis (ICA) on the Sentinel-1 data to (a) reduce noise before modeling and (b) test the independence of displacements in different parts of the Timanfaya lava fields. Independent component analysis decomposes mixed signals into statistically independent components, and is useful for separating volcanic, tectonic or hydrological deformation from atmospheric noise in multi-temporal InSAR (Ebmeier, 2016; Gaddes et al., 2019; Maubant et al., 2020; Peng et al., 2022). Random variables are decomposed into a linear combination of components that are statistically independent in space or time (Comon, 1994; Hyvärinen & Oja, 1997), based on the assumption that constituent components are non-Gaussian.

Here we used spatial ICA to analyze the Timanfaya displacements using the fast fixed-point algorithm (FastICA, Hyvärinen and Oja (1997)). Since the displacement rate is constant through time, we maximize the signal-to-noise ratio by applying spatial ICA to longer timespan interferograms, initially the set of 1-year images used to
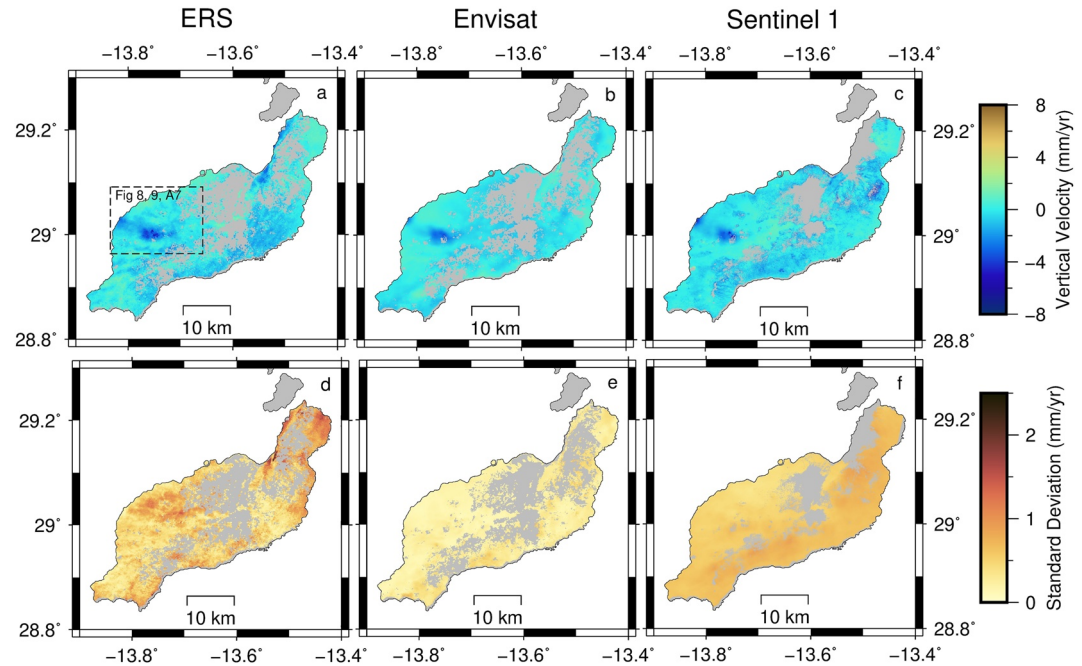
Figure 7. Vertical component of deformation for each of the various periods of Interferometric Synthetic Aperture Radar covered by pixels coherent in both ascending and descending directions (note for the European Remote-Sensing Satellite (ERS) estimate of vertical velocity based only upon a single look direction, all line-of-sight motion on the descending track was resolved into the vertical component). (d–f) Shows the corresponding standard deviations of the velocity calculated in LICSBAS (Morishita et al., 2020) from the cumulative displacements using a percentile bootstrap method.

produce the stacks in Figures 2g and 2h. We improved our results further by constructing all possible independent 3-year stacks (almost the full duration of the Sentinel-1 data set). Using these for retrieval of independent components reduces the number of contributions from noise due to multiple varying atmospheres from each individual epoch. We also masked out areas of lower coherence (<0.35) to minimize the impact of any small residual unwrapping errors that occurred over very steep topography in some individual interferograms. We reduced the number of dimensions of our datasets by removing the smallest principal components (to 15 for the ascending and 21 for descending) during preparation for ICA, and retrieve 10 and 16 independent components for the ascending and descending datasets respectively. The numbers of components were selected iteratively (Ebmeier, 2016), so that (a) the distinctive Timanfaya subsidence always appears as an independent component and (b) the fixed point iteration consistently converges. As the FastICA algorithm uses a random starting point for estimation of each unmixing matrix row (Hyvärinen & Oja, 2000), the order of independent components retrieved is arbitrary and unrelated to their significance. Similar independent components retrieved from multiple retrievals (restarts of the FastICA algorithm) are therefore most likely to represent a significant property of the input data set. We used 50 runs for each of the ascending and descending datasets, each time identifying the components containing the Timanfaya subsidence on the basis of its spatial pattern. By taking the mean of the velocity fields reconstructed from each of these (Figures 8a and 8d), we obtained a slightly cleaner velocity field for modeling (Figures 8a–8f), with variances of 0.32 mm^2 (ascending) and 0.18 mm^2 (descending), relative to 0.35 mm^2 (ascending) and 0.42 mm^2 (descending) for the stack of 1-year interferograms (distribution of variances in data reconstructed from 50 restarts is shown in Figure 8g).

3. Results and Interpretation

There is a consistent vertical deformation signal across much of the Timanfaya National Park lavas of about 2–6 mm/yr (Figure 7). The main part of the signal is approximately circular, 3–4 km in diameter and centered just to the south-west of the Islote de Hilario visitor center. However, the subsidence pattern also extends to the northwest toward the coast where further subsidence of ~4 mm/yr is observed at the coastline (Figures 7a–7c) in all velocity maps. The area where significant subsidence is observed above the background measurement noise
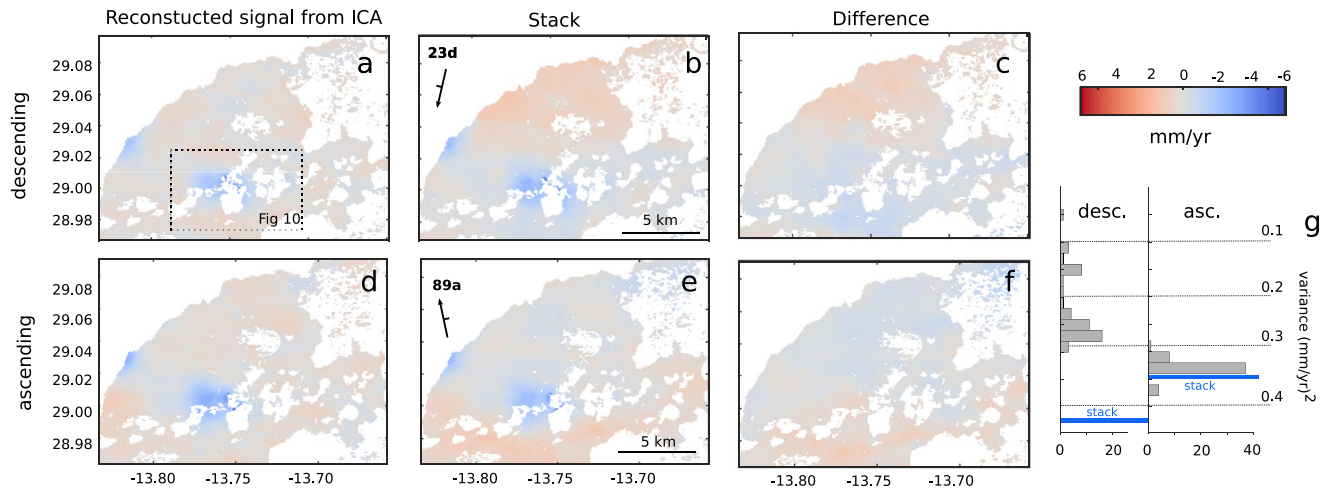
Figure 8. Mean displacements of 50 reconstructions of independent components for the descending (a) and ascending (d) datasets. The Independent Component Analysis reconstruction has a lower variance than the stacks of independent 1 year interferograms (b and e) and residuals between the stack and the reconstruction (c and f) are spatially correlated on the km scale. The distribution of variances of displacements reconstructed from selected independent components for each of 50 restarts are shown in (g), relative to the variance for the stacks of 1-year interferograms (b and e).

is about 20 km^2. Immediately on and around Islote de Hilario, larger magnitude but much shorter-wavelength (100 m scale) subsidence signals of 8 mm/yr are observed. These higher subsidence rates are centered on the location of previously measured temperature anomalies (Figure 1) (Araña et al., 1984; González & Fernández, 2011). Time series analysis shows that the deformation rates observed across the Timanfaya area have been consistent within uncertainty across the three decades of observation from ERS, ENIVSAT and Sentinel-1 (Figure 9).

The independent components corresponding to the Timanfaya subsidence have a distinctive spatial pattern, with both the long-wavelength region encompassing the present day visitor center (Islote de Hilario) and those on lava flows to the north-west at the coast consistently retrieved in the same component (Figure A8). We are confident that this captures all of the long-wavelength subsidence signal identified from the time series and stack, because reconstructed interferograms produce very similar velocities to those shown in Figure 2. We effectively exclude from our modeling the very localized patches of higher magnitude subsidence at Islote de Hilario by masking out lower coherence pixels. That both the broader subsidence around Islote de Hilario and the patch at the coast are decomposed into the same component is a robust indication that the two processes are correlated.

Subsidence in a post-eruptive period has been attributed to a range of processes related both to volume changes in a magma reservoir (e.g., Hamlyn et al. (2018)) and to alteration of new flows and substrate (Ebmeier et al., 2012; Stevens et al., 2001; van Wyk de Vries & Matela, 1998). While some causes for subsidence, such as gas loss from an isolated reservoir, may end within months to years, others may persist for decades to hundreds of years in particular conditions. We discuss the range of possible explanations for long-term subsidence in Section 4, but select two scenarios for exploration with geodetic and thermal models: (a) the crystallisation-driven contraction of a sill intruded during the Timanfaya eruption, and (b) the thermoelastic contraction of the Timanfaya lava flows.

3.1. Crystallisation of a Sill

3.1.1. Deformation Source Geometry

To test the possibility of the Timanfaya subsidence being caused by the thermal contraction of a magma body, we retrieved a first order approximation of the geometry of any subsurface deformation source using elastic half space models. We focused on the large patch of subsidence surrounding Islote de Hilario as the most probable location of a magmatic intrusion. We modeled the line-of-sight displacement rates reconstructed from our ICA analysis as the uniform closing of a sill (Okada, 1985) using a Bayesian approach to inversion (Bagnardi & Hooper, 2018) of the source parameters using their prior probability, and uncertainty characterized by the variance-covariance matrix of the InSAR data. This approach provides an estimation of posterior probability
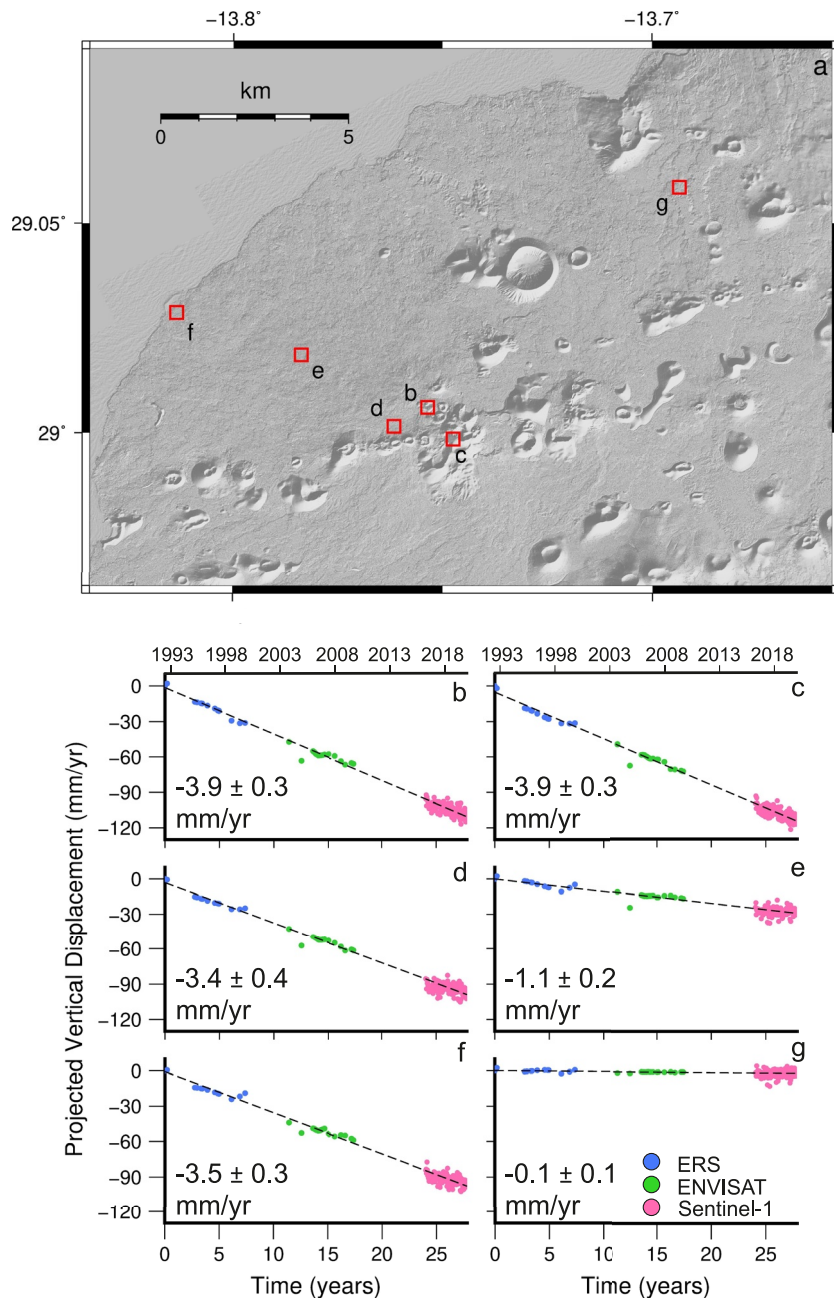
Figure 9. For six chosen localities across the Timanfaya area of Lanzarote shown in (a), time-series plots of the descending line-of-sight displacements projected into the vertical direction are shown (b–g) for comparison across the three time periods of Interferometric Synthetic Aperture Radar datasets. The time starts from the first European Remote-Sensing Satellite (ERS) acquisition on 2 September 1992 and the calculated velocities are for a linear fit through the three time series datasets from pixels averaged over a square region ∼300 m in extent.

density functions of the source parameters based, in our case, on the data uncertainty characterized by the variance-covariance matrix of the InSAR data and a uniform prior. We downsampled every set of reconstructed displacements in a bounding box extending from −13.79 to −13.71°E, and 29.02–28.97°N, using a reference point at −13.79°E, 29.03°N for the local Cartesian coordinate system. This downsampling is conducted using a quadtree algorithm (e.g., Bagnardi and Hooper, 2018) to produce datasets of approximately 1250 points in each of our four datasets. Prior to inversion, we characterized spatially correlated errors by fitting an experimental semivariogram; the corresponding values for sill, range and nugget for each data set can be found in the Appendix
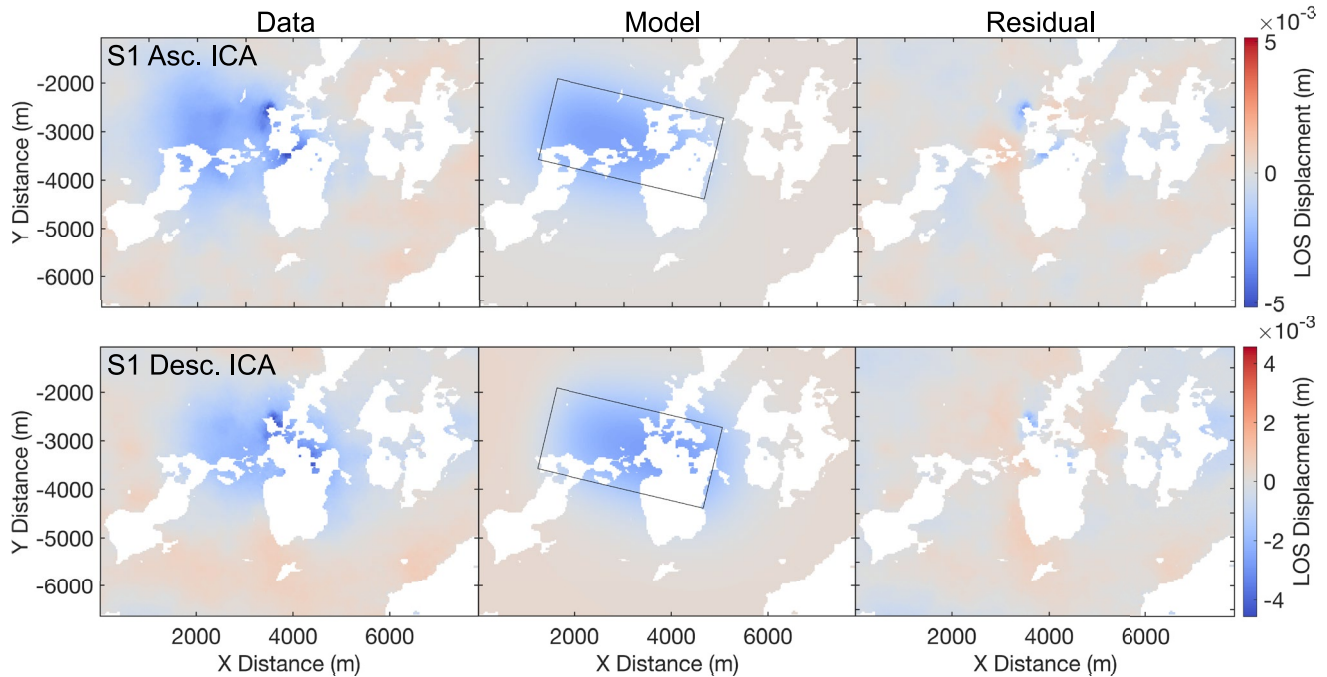
Figure 10. Best fit sill models and residuals using Geodectic Bayesian Inversion Software for the displacement observed at Timanfaya in the Independent Component Analysis (ICA) reconstructed line-of-sight velocity datasets. Note positions are relative to an arbitrary origin point −13.79°E, 29.03°N. The upper row shows the data, model, and residual for the ascending track, while the lower row shows the same for the descending track. The spatial geometry for the optimal model is illustrated as a black rectangle, in the "Model" panel of each row. The results for the stacked data set can be found in Appendix (Figure A9).

(Table A2). We performed a joint inversion using both ascending and descending data. We find the best fitting sill geometry by allowing the X (Easting) and Y (Northing) values to vary across the subsiding area of the Islote de Hilario signal (origin distance of 100–5000 m, and −4500 to −1500 m, respectively). We searched across a range of 100–10000 m for both sill length and width, and between 1 and 359° for sill strike. Finally, we allowed sill opening to vary between −5–5 m/yr, across a depth range of between 250 and 5000 m. We iterated 1×10^6 times, and discarded the initial 5×10^4 iterations as a "burn-in" time. The estimated parameters are presented in Table A3, while the input data, modeled sill, and residual in both track directions, are presented in Figure 10 for the ICA reconstructed data and Figure A9 for the stack data. Histograms of posterior density functions for each source parameter for the stacked data set (Figure A10) and for the independent component analysis data set (Figure A11) are shown in the appendix.

The majority of Islote de Hilario deformation in the Sentinel-1 era can be acceptably explained by the ∼10 mm/yr closing of an approximately WNW-ESE orientated sill in the upper 2 km of the crust. The best-fit parameters found for the ICA reconstructed signal have a narrower acceptable range (Table A3) than those from the stack of 1-year images (Figure A9), presumably due to the reduction in data variance in the ICA analysis. For example, the stacked data set has posterior ranges (between the 2.5 and 97.5 percentile) of approximately 764 and 269 m of posterior length and width, respectively. These ranges reduce to 221 and 113 m in the ICA data set. Additionally, the posterior distribution is much more tightly and normally distributed for the length and opening in the cleaner ICA version (Figure A11) than for the original stacked data set (Figure A10). The full range of values are presented in Table A3.

3.1.2. Thermal Modeling

We used our best-fit source geometry to test whether the broader contemporary subsidence could be caused by cooling and crystallisation of a sub-volcanic magmatic intrusion dating from the 1730s Timanfaya eruption. An anhydrous magma, where no fresh influx of magma is occurring, will contract as denser-than-melt crystals form during cooling (e.g., Caricchi et al., 2014; Okmok 2014), causing surface subsidence. We assessed the potential contribution of magma crystallisation to the Timanfaya surface deformation, by first calculating volume change for a magma cooling from liquidus to solidus. Using MELTS phase equilibria software (Ghiorso & Gualda, 2015;

Table 3
Physical Parameters Used in Crystallisation and Lava Subsidence Modeling

Variable	Symbol	Value	Units	Reference
Thermal Conductivity[a,b]	k	2.5	$Wm^{-1}K^{-1}$	Annen (2017)
Density[b]	ρ	2500	kgm^{-3}	Annen (2017)
Specific Heat[b]	c_p	1000	$Jkg^{-1}K^{-1}$	Annen (2017)
Latent Heat [a]	L	3×10^5	$Jkg^{-1}K^{-1}$	Annen (2017)
Emissivity[b]	ϵ	0.95	–	Patrick et al. (2004)
Stefan-Boltzmann constant[b]	σ	5.67×10^{-8}	$Wm^{-2}K^{-4}$	Patrick et al. (2004)
Convective heat transfer coefficient[b]	h_c	75	$Wm^{-2}K^{-1}$	Patrick et al. (2004)
Thermoelastic expansion coefficient[b]	η	3.4×10^{-5}	K^{-1}	Chaussard (2016)
Poissons ratio[a,b]	ν	0.25	–	Chaussard (2016)
Initial Lava temperature[a]	T_L^0	1200	°C	–
Ground temperature[b]	T_G^0	25	°C	–
Ambient temperature[b]	T_a	20	°C	–

[a]Crystallisation Model. [b]Lava model.

Gualda et al., 2012), we calculated the change in system density for a representative Timanfaya basalt (Solana et al., 2004b). We then determined cooling timelines for these volume changes, using the 1-D finite-difference heat equation (Equation 1), for example, Annen (2017)), assuming that all heat loss occurs through conduction. Here, c_p is specific heat, T is temperature, t is time, L is latent heat, X is melt fraction, k is thermal conductivity, and x is distance. c_p and ρ, as well as the solidus and liquidus temperatures, are calculated from the MELTS simulation. Independent variables are presented in Table 3.

$$\rho c_p \frac{\partial T}{\partial t} + \rho L \frac{\partial X}{\partial t} = k \frac{\partial^2 T}{\partial x^2} \tag{1}$$

Although we used an Okada model to initially find the best-fit subsurface geometry (Section 3.1.1), this is not appropriate for predicting displacements from an isotropic process such as crystallisation-driven contraction. We therefore used point Compound Dislocation Models (pCDMs) (Nikkhoo et al., 2017) to calculate the change in surface displacement with time. To model this crystallisation in a sill geometry, we discretized the intrusion onto a uniform grid of equal length and width. We placed a pCDM at the centroid of each point in the grid, and calculated the resulting displacement at the surface. We calculated the superposition of displacement of the sill throughout time, to construct predicted time series of displacement due to crystallisation. We took the geometry of the sill (depth and width) from the acceptable ranges predicted by the simple elastic half space inversion described in Section 3.1.1. We placed the sill at 1700 m depth, with equal length of 1600 m (allowing us to discretize our sill, while conserving sill surface area). These values approximate those found by inverting the stacked Sentinel-1 data, which are deeper than those found during the inversion of the ICA data. By doing so, ambient country rock temperatures around are increased, and the emplaced sill will take longer to crystallize. We note that the depth found from our ICA results would result in even faster cooling, requiring an even thicker sill, which makes this model less likely. Thermal parameter values, alongside a conceptual model of the modeling scenario are presented in Figure 11. We systematically varied the thickness of the emplaced magma (between 10 and 200 m, see Figure 11b), along with the geothermal gradient. We varied this from 25°C/km, the average geothermal gradient, to 300°C/km, so that the ambient temperature at the depth of emplacement is similar to the >600°C thermal anomaly identified by Araña et al. (1984). Though this end-member is unrealistically high (the basaltic liquidus would be reached at 4 km depth), we used it here as a conceptual scenario where such extreme anomalies affect the cooling of an intrusion.

For crystallisation to produce surface displacements, the sill must remain above solidus temperature, so that density changes can still occur as crystals solidify. Parameter testing showed that a sill at least 200 m thick, intruded into a geothermal gradient of at least 100°C/km (four times the normal continental gradient of 25°C/km) is required in order for any melt to remain in the sill during our period of measurement. A sill this thick is
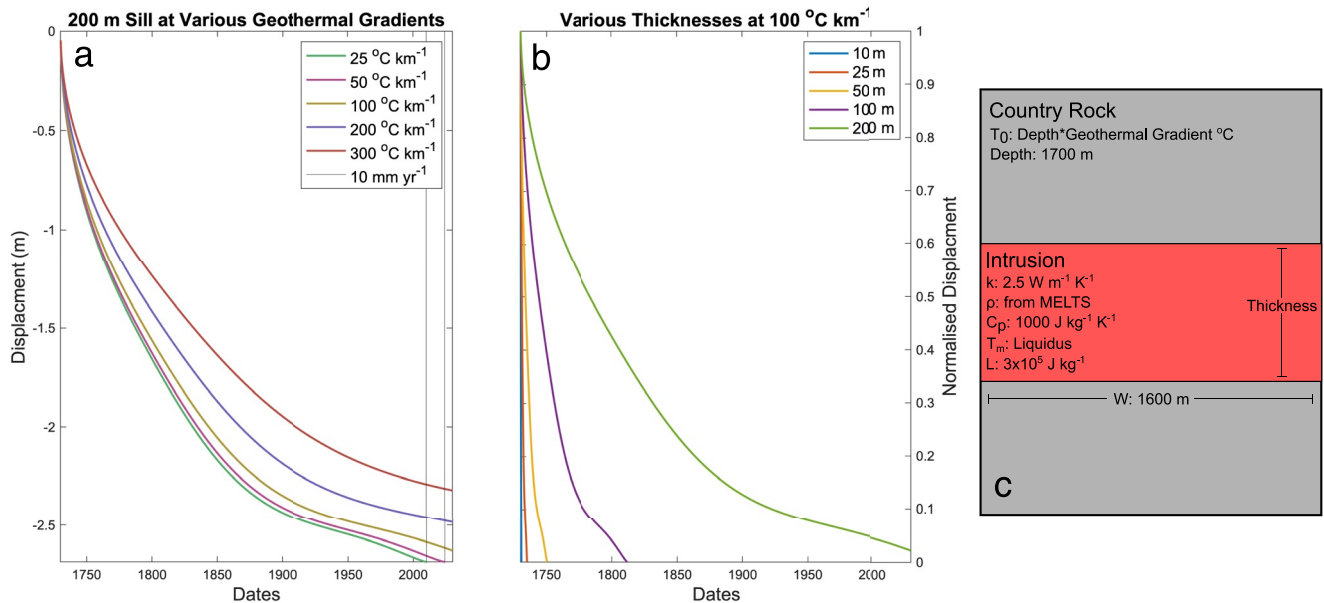
Figure 11. Time series of displacement from cooling and crystallisation of a shallow sill (1700 m depth to mid-point). Volume change with time is predicted using MELTS phase equilibria software, alongside a 1D thermal model, and a displacement forward model. (a) A 200 m thick sill cooling under a range of geothermal gradients, shown by the inset colors. The black lines indicate the point at which deformation of 10 mm/yr would be observed. (b) Normalized displacement with time for an array of sill thicknesses, under constant geothermal gradient. A thickness of 200 m is required for the magmatic intrusion to remain greater than the solidus temperature in the 21st century. (c) Schematic of the model setup in cross section view. Gray areas are country rock while the red area is the magma intrusion. Intrinsic parameters are labeled. Intrusion thickness and geothermal gradient vary with each model run, while density varies with temperature, as predicted by MELTS.

unrealistic (Button & Cawthorn, 2015), especially given the lack of evidence of a magma reservoir from gravity measurements (Camacho et al., 2019). Our simple modeling assumes that the sill was intruded as a single unit during the Timanfaya eruption, which is not consistent with understanding of how magmatic zones develop from multiple successive episodes of intrusion (Annen, 2017), nor with magnitudes of opening during recent major intrusions (Wright et al., 2006). However, the assumption of a sill of uniform age and properties, while unrealistic, gives us an indication of the minimum intrusion thickness and geothermal gradient required for remnant magma from the 1730s to still be crystallizing. Although it is possible that the Timanfaya subsidence could relate to more recent magma ascent, there has been no geophysical evidence of intrusions at Timanfaya in the 20th or 21st centuries (Rueda et al., 2020). We therefore consider it highly unlikely that the Islote de Hilario subsidence is primarily driven by the cooling of a subsurface intrusion.

3.2. Lava Cooling and Subsidence

Large outpourings of lava occurred in the first few months of the Timanafaya eruption (Carracedo et al., 1992). While individual flows were relatively thin, accumulation of multiple flows, and especially infilling of topographic lows, have the potential to build up thicker layers of lava.

We predicted surface displacements due to thermal contraction of the Timanfaya lava field with numerical calculations, using the partial differential equation toolbox, in MATLAB R2021b. We assumed that heat transfer between the lava flow and underlying country rock is through conduction, with the exclusion of latent heat release, such that $q_k = k \left(\frac{\Delta T}{\Delta x} \right)$. Here, q_k is conductive heat flux, k is thermal conductivity, and $\frac{\Delta T}{\Delta x}$ is the thermal gradient (e.g., after Chaussard, 2016; Patrick et al., 2004). The values used for independent variables are presented in Table 3. Heat loss at the lava surface was modeled by imposing a radiative-convective boundary condition. Radiative heat loss is given by $q_r = \epsilon \sigma \left(T_l^4 - T_s^4 \right)$, where q_r is radiative heat flux, ϵ is lava surface emissivity, σ is the Stefan-Boltzmann constant, and T_l and T_a the lava and ambient, temperatures, respectively. Convective heat loss is given by $q_c = h_c(T_l - T_s)$, where q_c is the convective heat flux, and h_c is the heat transfer coefficient. The values assigned to each of these variables is given in Figure 12, where an illustration of the model
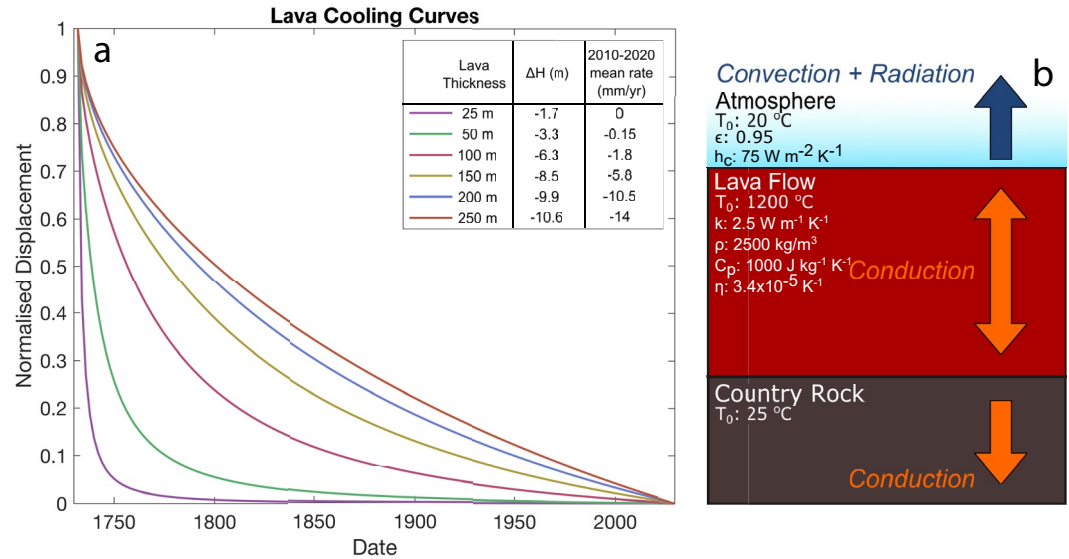
Figure 12. Time series of displacement for a cooling lava flow. (a). Cooling curves for lava flows of various thicknesses (25–250 m). Normalized displacement is presented on *y*-axis to allow all curves to be presented on the same plot. We assume the lava flows were emplaced during the 1730 eruption of Timanfaya; time since then is presented on the *x*-axis. Line color represents the thickness of lava flow at time on emplacement. The inset table presents the initial lava flow thickness, the total ground deformation since emplacement (ΔH), and the average rate, in millimeters per year that was observable in the past decade (covered by the Sentinel-1 data analyzed here). The model is constructed using the MATLAB partial differential equation toolbox. (b). Conceptual model of our modeling setup. Heat loss occurs as conduction within the lava flow, and in the country rock that it is emplaced upon. We use a radiative-convective boundary condition on the upper surface of the lava flow to account for heat loss into the atmosphere.

set up is also described. We neglected the effects of bubble vesiculation, and fixed the ambient temperature to 20°C (the average annual temperature in Lanzarote). Displacement change, driven by thermoelastic contraction of the lava flows, is calculated by $\Delta h(t) = h\eta \left[\frac{1+\nu}{1-\nu} \right] \Delta T(t)$ (e.g., Chaussard, 2016). Here, Δh is height change, η is the thermoelastic expansion coefficient, ν is Poisson's ratio, T is temperature, and t is time. Using this approach, we modeled ground surface displacement with time, for lava thicknesses between 25 and 250 m thick. We emplace the lava flows at 1200°C (liquidus temperature of basalt), and calculated the resulting displacement change in 2 year increments, for 300 years. We systematically varied the thickness of the emplaced lava to identify the thickness required to produce the observed displacement rates.

We found that a minimum lava emplacement thickness of approximately 150 m is required to reproduce the current subsidence rates of ~6 mm/yr observed over significant areas of the Timanfaya lava flows (Figure 12). With this starting thickness, average subsidence rates due to thermoelastic contraction of 6 mm/yr were predicted between 2010 and 2020 and would be similar for the preceding two decades and the next (Table 4). Note that these estimates are minimum values, as we have neglected additional processes (e.g., latent heat of crystallisation, thermal advection due to ground water circulation, and bubble vesiculation) that would result in faster cooling. Thickness of 25, 50, and 100 m are insufficient to recreate the observed deformation, while thicknesses of 200 and 250 m produce average rates of >10 mm/yr, exceeding the current observed rates. This suggests that lava thicknesses in the subsiding areas may be of the order 100–150 m within the national park and nearly as much toward the coast where up to 4 mm/yr of subsidence is observed. This suggests that previous lava flow observations at the coast to the West (Sharma, 2005) may not be sampling the thickest accumulations of lava which we estimate here to be twice as thick as those previous 30–50 m measurements which were from a less effusive stage of the eruption.

Table 4
Modeled Average Decadal Vertical Deformation Rates (mm/yr) for Thermal Contraction of Varying Lava Flow Thicknesses Emplaced in the 1730–36 Eruption

Thickness (m)	1990–2000	2000–2010	2010–2020	2020–2030
25	−0.01	−0.01	−0.01	−0.01
50	−0.17	−0.16	−0.15	−0.13
100	−2.06	−1.91	−1.77	−1.65
150	−6.54	−6.13	−5.77	−5.44
200	−11.60	−11.05	−10.54	−10.07
250	−15.48	−14.91	−14.37	−13.86

4. Discussion

We consider the best explanation for the long lived Timanfaya subsidence observed here to be the thermal contraction of the lava flows from the 1730s eruption. First, the subsidence signals are located over the site where we expect the thickest lava flows to reside. Reconstructions of successive eruption phases by Carracedo et al. (1992) indicate lavas initially flowing out predominately to the north-west covering a large area in the first couple of months of volcanism. Then again in 1732, voluminous lava flow outpourings are reported to have occurred and it is suggested that these followed topographic lows, infilling pre-existing wide valley floors down to the sea (Carracedo et al., 1992).

Second, the pattern of displacement is discontinuous, extending 6–7 km from near the current visitor center out to the coast, with local maxima centered south-west of Islote de Hilario and at the coast. This is consistent with subsidence originating within 10–100 s m of the Earth's surface, rather than at kilometres depth which would produce a much smoother signal. We are confident that both the coastal and larger central Timanfaya subsidence are related to the same process because they are consistently retrieved in a single independent component from ICA decomposition of several dozens of independent interferograms. Subsidence related to loading of the substrate below the 1730s lavas would also be more spatially extensive, so we do not consider this to be a plausible explanation. We attribute the subsidence found here to the 1730's eruptive phase rather than the more recent 1824 eruption as the latter was much smaller, and the only significant lava outpourings from this later eruption flowed due north from a cone 500 m north of Islote de Hilario, so is not associated with the area of measurable subsidence.

Elastic dislocation modeling of the section of the subsidence signal at Islote de Hilario using a sill source model is consistent with the continued but slow closing of a kilometer scale sill at 1–2 km depth beneath Timanfaya (see Table A2). Such a sill was previously put forward as a possible source based upon the ERS data from the 1990's (González & Fernández, 2011). However, our observations from the following two decades show a remarkably consistent rate of subsidence (Figure 9), which is improbable for such a shallow sill, especially as there is no evidence for an intrusion in the decades before the ERS observations of subsidence (González & Fernández, 2011).

We consider it highly unlikely that the subsidence originates from the cooling of an intrusion emplaced during the 1730s eruption, as this would have required a much thicker intrusion of juvenile material than previously observed in geodetic data and from field studies. We cannot rule out the possibility that clast repacking or gravity-driven compaction also contribute to the subsidence. However, we note that this is less likely for a basaltic than andesitic, blockier flows emplaced on steep slopes. Measurements of displacement attributed to clast repacking have thus far been made only shortly after flow emplacement and over months to years (Ebmeier et al., 2012; Schaefer et al., 2016).

The very short wavelength (few hundred meters) higher subsidence rates of more than 8 mm/yr observed immediately around the visitor center and also 1 km to the South-South East of this (as seen in the Geodectic Bayesian Inversion Software residuals Figure 10) may be associated with particularly thick accumulations of lava. However, both regions of highest subsidence are also associated with the highest heat flows (Figure 1c) and therefore the higher subsidence rates may be the result of overprinting of minor deformation from more efficient lava contraction along permeable pathways within the eruptive products or vents. Contraction of a cooling sill would also produce only longer wavelength signals and cannot explain the localized higher-rate displacements around the visitor center.

Previous literature estimates of the greatest thicknesses for the 1730s flows are of only a few tens of meters (10–60 m (Araña et al., 1973) and 30–55 m for coastal sections where 2–3 units are vertically stacked (Sharma, 2005)). If the 100–150 m thickness suggested here are correct for a significant portion of the Timanfaya lavas in the north-west of the island, the onshore volumes may be significantly larger than those previously estimated from Carracedo (2014) of 3–5 km^3 and 5.32 $\pm$ 1.35 km^3 from Sharma (2005). Given the 1730s lava flow area is at least 200 km^2 in subaerial extent, the average flow thickness based on those previously reported volumes would be <25 m.

Such potentially thick lava thickness values are consistent with those observed elsewhere in previous studies of lava effusions. Chaussard (2016) found that subsidence rates of 55 mm/yr in the Parícutin lava field can be

explained by contraction of a 200 m thick lava flow, emplaced 60 years before the period of observation. In the Canary Islands, recent eruptive products from the 1971 Teneguia volcano eruption in La Palma has been observed to still be subsiding (González et al., 2010). Additionally, given that the original coastline on Lanzarote may well have been built out an additional couple of kilometres to the north-west over the course of the eruption (IDECanarias visor 4.5.1, n.d.), there could be significant additional volumes of lava below sea level filling up the Island's shallow waters platform (100 m). The recent eruption at La Palma (2021), which despite being much smaller (0.19 km^3) and lasting only 85 days, saw significant thicknesses of lava of >50 m accumulating at the coast (Carracedo et al., 2022) as they flowed over the pre-existing cliffs and built out the western coastline there. The coastal subsidence found here on Lanzarote may delineate where the pre-eruption coastline originally ended and a similar process of lava flow accumulation occurred, shifting out the coastline. Additionally, the relatively short eruption and low volumes of the Cumbre Vieja Volcanic Ridge eruption on La Palma was still able to accumulate flows of at least 50 m thickness in the center of the lava fields (as well as around the vents).

Whilst the lava volumes may be significantly larger than previously thought, it is unlikely that the 1730s outpourings were as voluminous as either of the pair of Icelandic eruptions from 1783 to 84 at Laki (Gudmundsson et al., 2008) or the earlier 934–940 Eldgjá eruption (Sigurardóttir et al., 2015). However, consideration of a greater erupted volume (especially the unknown amount of submarine volumes from building out of the coastline to the northwest) has potential implications for accurately constraining the environmental impact of the eruption and volcanic loading for climatic simulations of atmosphere perturbations (Pausata et al., 2015; Yang et al., 2019), or Canary Islands eruptive hazard assessment (Longpré & Felpeto, 2021).

For the range of thicknesses estimated here of the order of 100 m, the changes in rates of subsidence for lava cooling are unlikely to be discernibly different across the decades compared to the level of noise. Only the thickest of lavas, if they were to have exceeded 150 m, could have resulted in 1 mm/yr difference across four decades (Table 4). Given the noise in the InSAR time series data, it is not possible to see a decreasing trend in the velocity across the InSAR datasets (Figure 9), although for the rest of this decade the average rate expected to be observed in the areas of faster subsidence surrounding Timanfaya with Sentinel-1 would be 0.4–1 mm/yr slower than that observed in the 1990's by ERS.

One of the limitations of high repeat SAR acquisitions in repeat pass interferometry is that the use of short time interval interferograms in the time series analysis has been shown to introduce a systematic bias (Ansari et al., 2021). We have explored that further here and demonstrated a strong bias that appears correlated with land cover that has a large impact on the measurement of small deformation signals. We have shown that for lava flows the impact of the phase bias is less. This suggests that the use of SBAS interferograms is still appropriate for other bare rock or dry areas such as the central Andes or Iceland. For other land cover types, where there is good coherence as in Lanzarote, we present an option to reduce the impact of the phase bias by creating networks of longer period interferograms (averaging more than 1 month). This is an alternative to correcting for the bias empirically (Maghsoudi et al., 2022). This bias was not apparent in the previously published ERS InSAR data (González & Fernández, 2011) as longer period interferograms formed the basis of their analysis.

5. Conclusion

We find that lava flows within the Timanfaya National Park, Lanzarote from the 1730–36 eruption exhibit continued subsidence rates of up to ~6 mm/yr. This has been consistently observed from earth observation satellite data from the past three decades using InSAR analysis to extract millimeter per year deformation rates across the entire island. The spatial pattern and magnitude of subsidence is most consistent with lava flow subsidence from emplaced flows due to the 1730–1736 eruption,which must be 100–150 m thick in places to still be significantly cooling and measurably subsiding. This ongoing deformation is the longest lived lava flow subsidence imaged to date of almost 300 years. Observation of such prolonged subsidence is an important factor to consider in ongoing analyses of sources of surface deformation associated with volcanoes in regions where there is the potential of thick lava flow accumulation in the past few centuries.

Appendix A: InSAR Analysis

Table A1
Selected Masking Threshold and Filtering Values Used in LiCSBAS Processing

Mask		Filter	
Coherence Threshold*	0.25	Spatial Filter (km)	2
Minimum Number Of Interferograms	$1.5 \times$ no. of epochs	Temporal Filter (days)	20
Standard Deviation of Velocity* (mm/yr)	10	Deramp Degree	1
Minimum Length of Longest Connected Network (years)	1	Linear Correction Min height* (m)	0
Maximum Number of Gaps in Network	10	Linear Correction Max height (m)	1000
Spatiotemporal Consistency (mm)	5	–	–
No. of Interferograms with Unidentified Unwrapping Errors*	1	–	–
Maximum Number of Unclosed Loops	5	–	–
Maximum RMS of Residuals in SB inversion (mm)	2	–	–

Note. * Denotes that the value was changed from LiCSBAS default value.

Table A2
Values of the Sill, Range and Nugget Used for Semivariogram Fitting in Geodectic Bayesian Inversion Software for Each Data Set

Data set	Sill (m^2)	Range (m)	Nugget (m^2)
ICA: Asc	5.3e−9	233	1.2e−19
ICA: Dsc	1.1e−8	258	1.8e−18
Stack: Asc	7.4e−9	502	9.3e−10
Stack: Dsc	9.4e−8	267	5.5e−17

Table A3
Optimal Geodectic Bayesian Inversion Software Results for Best Fitting Sill Model

Parameter (Unit)	Stack Optimal	Stack 2.5%	Stack 97.5%	Searchable Range
Length (m)	831	508	1272	100–10000
Width (m)	4091	3975	4244	100–10000
Depth (m)	1757	1605	1833	250–5000
Strike (°)	197.5	195.5	199.3	1–359
X[a] (m)	1190	1098	1267	100–5000
Y[a] (m)	−2402	−2493	−2316	−4500 to −1500
Opening (m/yr)	−0.014	−0.024	−0.008	−5–5
InSAR Const. Asc. (m)	4×10^{-4}	3.6×10^{-4}	4.4×10^{-4}	
InSAR Const. Dsc. (m)	1.3×10^{-4}	7×10^{-5}	2.1×10^{-4}	
Parameter (Unit)	ICA Optimal	ICA 2.5%	ICA 97.5%	Searchable Range
Length (m)	1712	1562	1783	100–10000
Width (m)	3533	3483	3596	100–10000
Depth (m)	1139	1096	1235	250–5000
Strike (°)	193.4	192	194.8	1–359
X[a] (m)	1432	1397	1463	100–5000
Y[a] (m)	−2742	−2784	−2654	−4500 to −1500
Opening (m/yr)	−0.006	−0.006	−0.005	−5–5
InSAR Const. Asc. (m)	3.1×10^{-4}	2.9×10^{-4}	3.4×10^{-4}	
InSAR Const. Dsc. (m)	1.5×10^{-4}	1.3×10^{-4}	1.8×10^{-4}	

Note. The Range That Each Parameter Was Allowed to Take Is Given in the Last Column. We iterated 1×10^6 times with a burn in of 5×10^4 iterations.

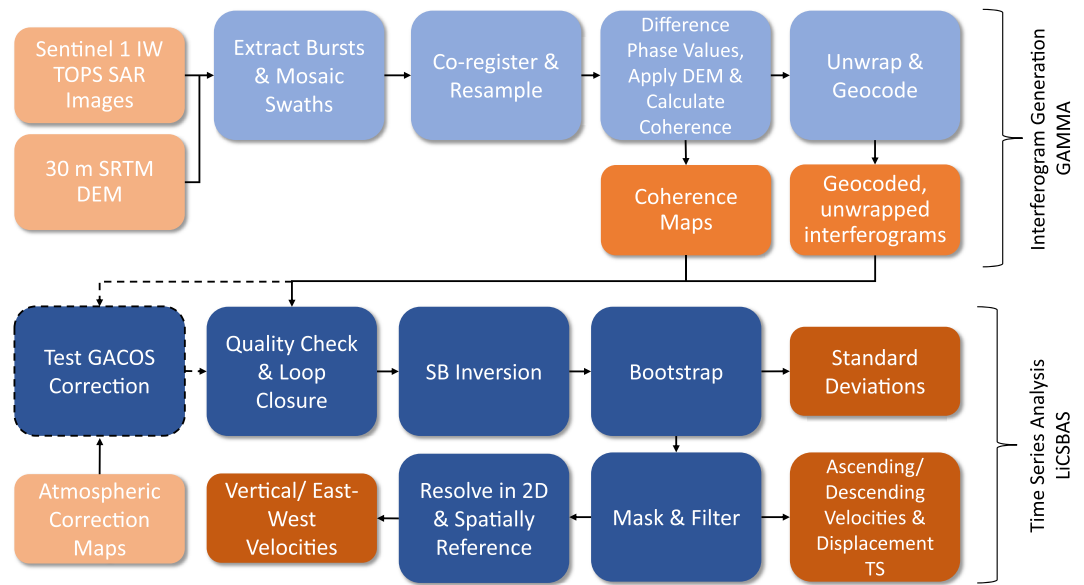[a]X, Y are positions relative to −13.79°E, 29.03°N.

Figure A1. Processing flow chart for derivation of Sentinel-1 time series to calculate surface estimates of velocities. The interferograms were created using GAMMA (Werner et al., 2000) and the time series analysis was completed in LiCSBAS (Morishita et al., 2020). Whilst used for comparison of atmospheric correction approaches, in the final velocity results, the Generic Atmospheric Correction Online Service for Interferometric Synthetic Aperture Radar (GACOS) correction step (C. Yu, Li, Penna & Crippa, 2018) was omitted and a linear correction with elevation was instead applied during the mask and filter step.
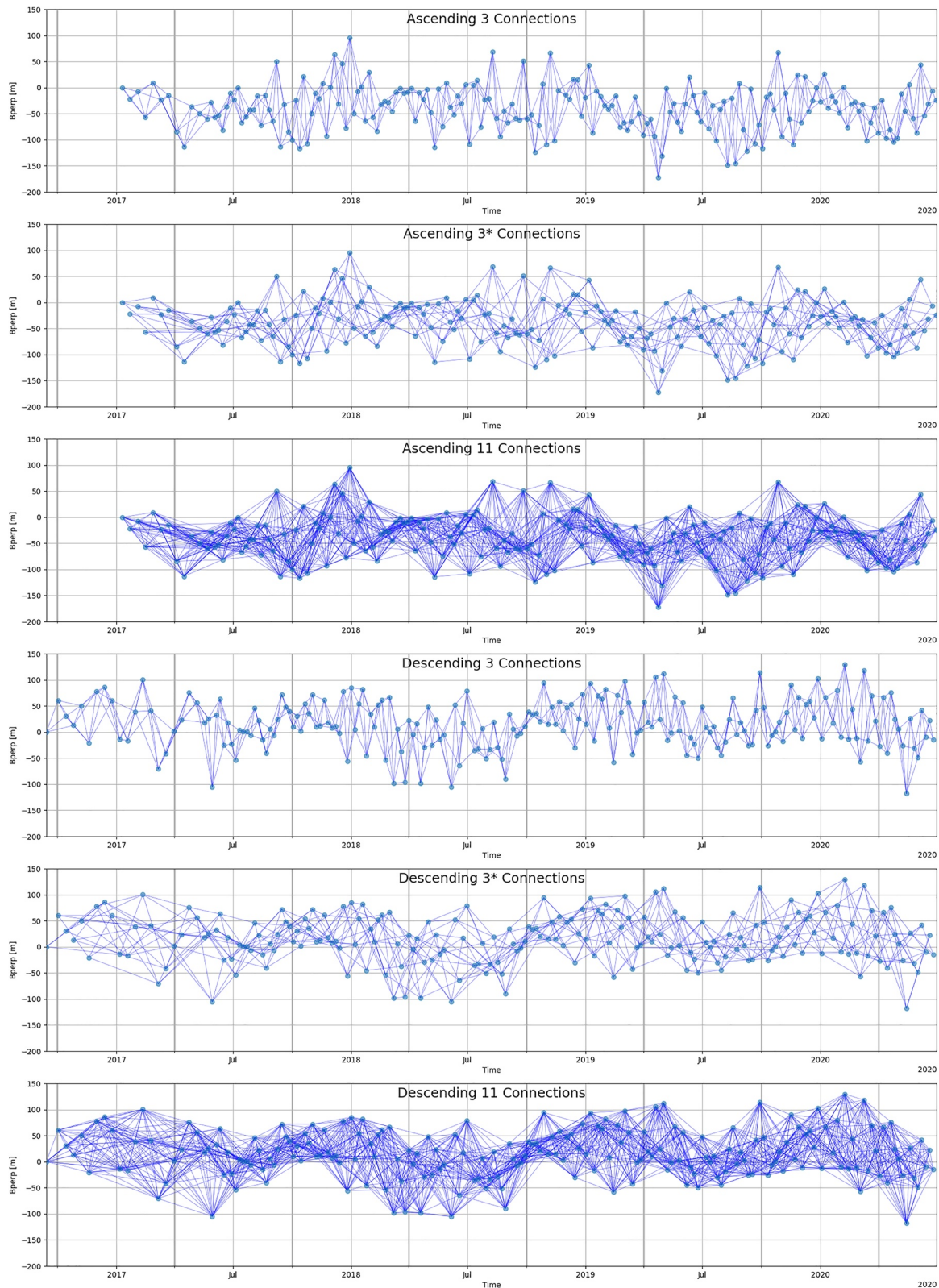
Figure A2. Perpendicular Baseline (Bperp) versus Time plot of Sentinel-1 interferogram networks for ascending track 089 and descending track 023 showing the difference between the most dense and sparse networks used in this study. Networks made in (a and d) are made with the 3 shortest forward connections from each epoch. Similarly (c and f) show the 11 shortest forward connections from each epoch. The networks in (b and d) have 3 connections from each epoch with longer interferogram lengths.
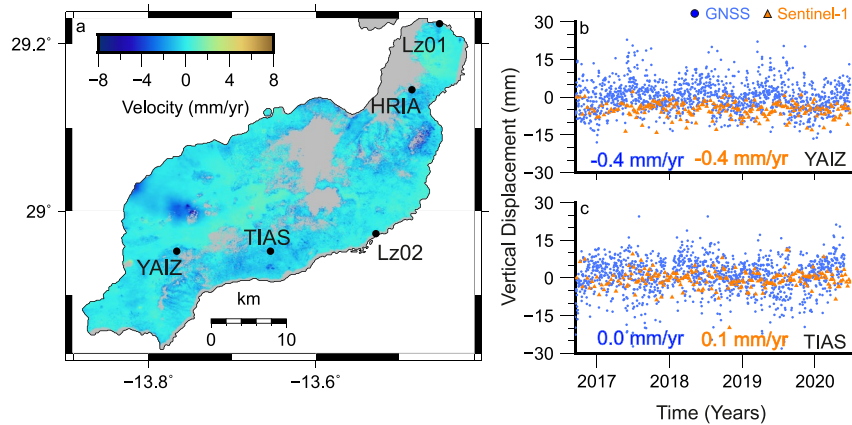
Figure A3. (a) Location of the five permanent Global Navigation Satellite System (GNSS) stations on Lanzarote with data openly available (Blewitt et al., 2018) from the Nevada Geodetic Laboratory (NGL). The GNSS vertical time series for the period of Sentinel-1 coverage from sites YAIZ (b) and TIAS (c) are shown as blue circles and the Interferometric Synthetic Aperture Radar (InSAR) time series are shown as orange triangles. The corresponding linear velocities are given under each time series. Note that the InSAR velocity averaged over a square region ∼200 m in extent around the GNSS site.
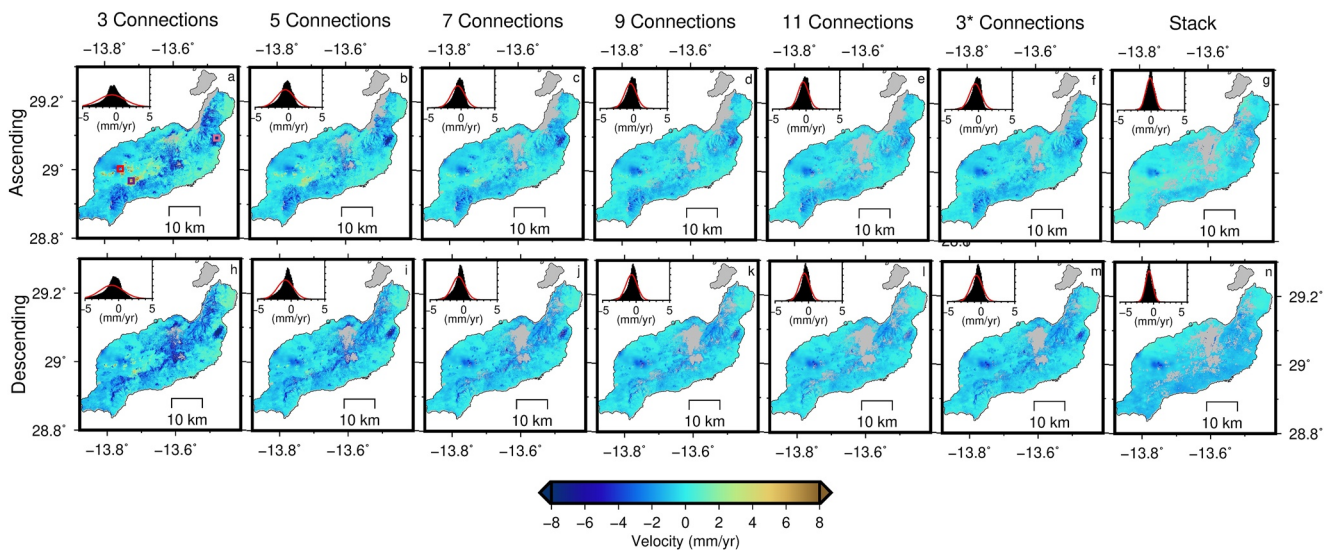
Figure A4. Sentinel-1 average line-of-sight velocity maps on ascending (upper row) and descending (lower row) orbits constructed from varying the number of network interferogram connections used in the time series inversion. The number of connections refers to the number of interferograms made from each epoch forward in time. The 3, 5, 7, 9, and 11 connection networks were made with the shortest possible interval interferograms. The 3* network had the same number of interferograms as the ordinary 3 connection network but with a longer average interferogram length. The final stack version was made by averaging all independent ∼1 year interferograms (right hand most column). Inset histograms in each panel show the distribution of the velocities and a normal distribution fit (red line).
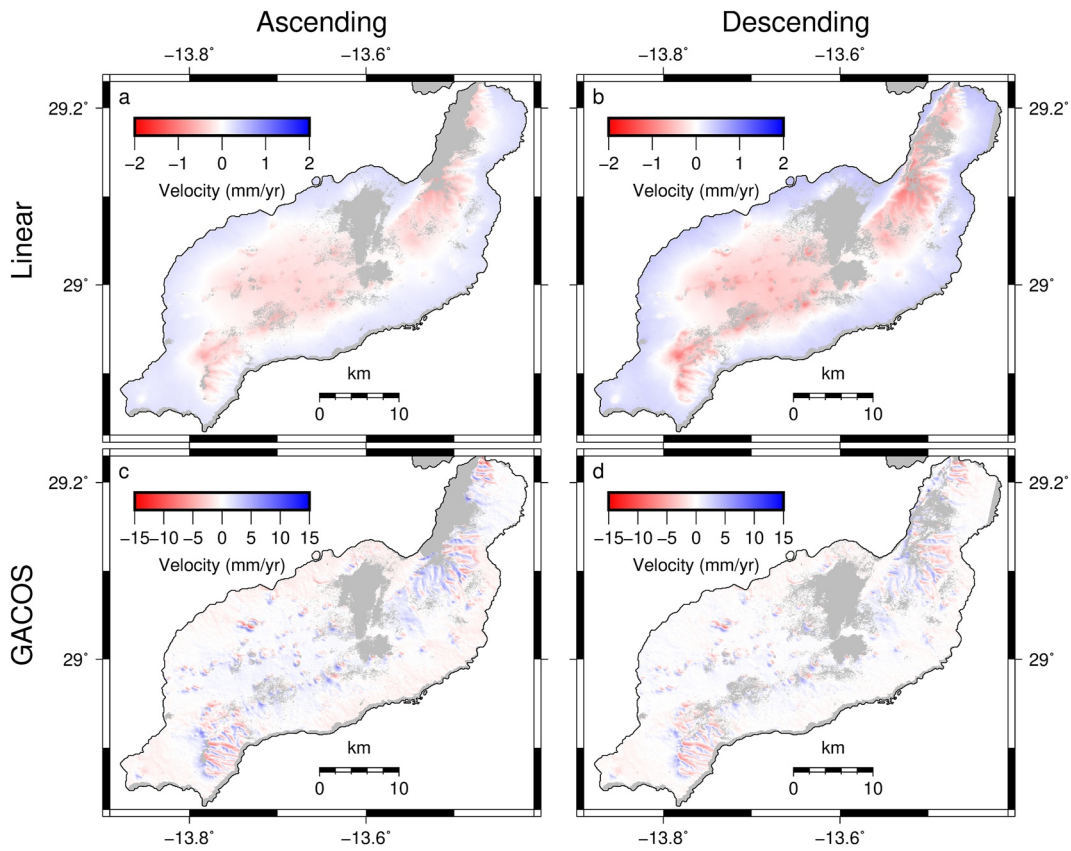
Figure A5. Residual differences in Sentinel-1 line-of-sight velocity maps from before and after applying a linear (a, b) or GACOS (c, d) atmospheric correction to the two look directions. Note the change in color scale in the residuals between the two correction approaches.
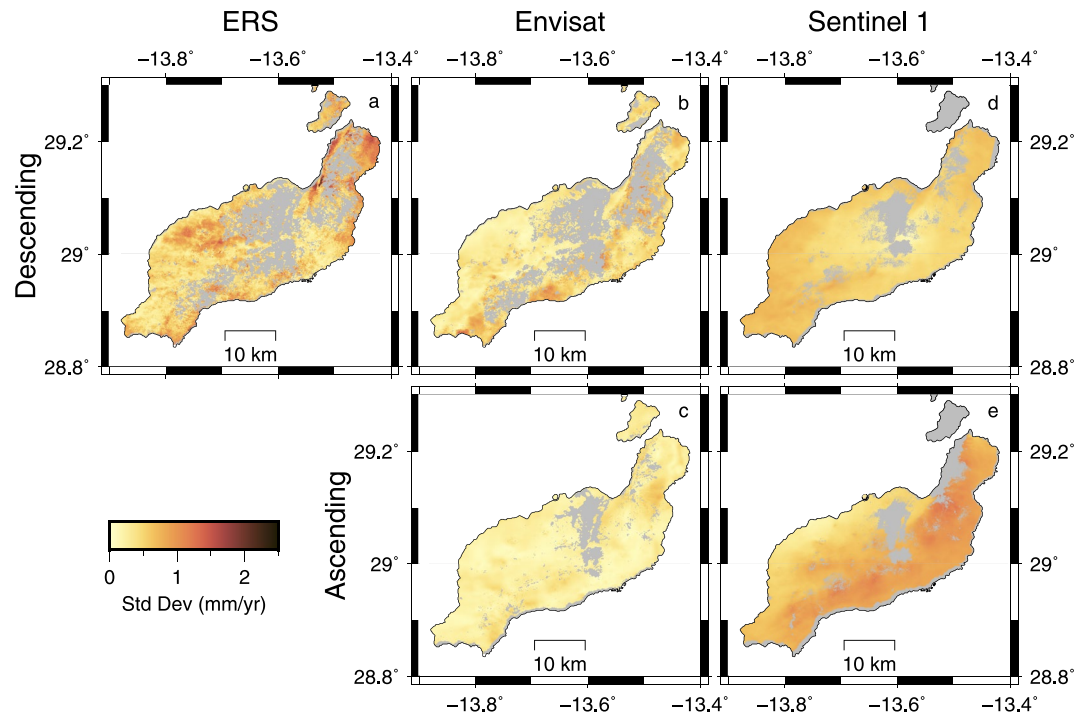

Figure A6. Standard deviations for European Remote-Sensing Satellite (ERS), ENVISAT and Sentinel-1 line-of-sight velocities calculated in LiCSBAS using a percentile bootstrap method.
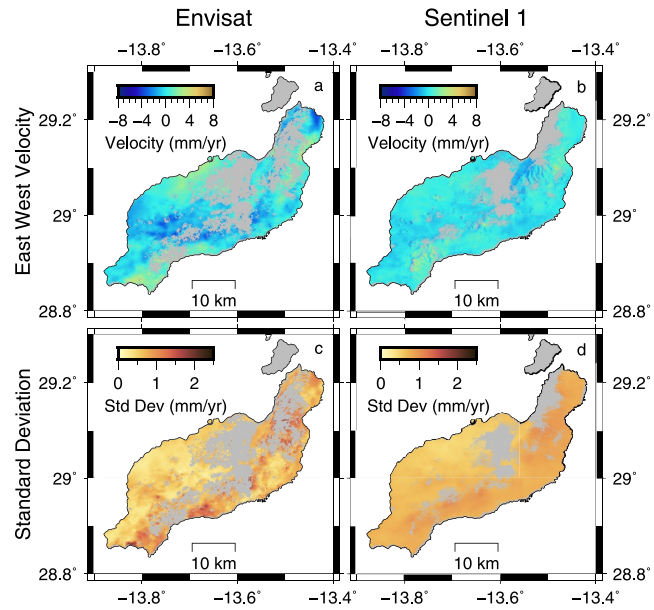
Figure A7. Retrieved east-west velocities from the decomposition of line-of-sight velocities from ENVISAT and Sentinel-1 and the corresponding standard deviations.
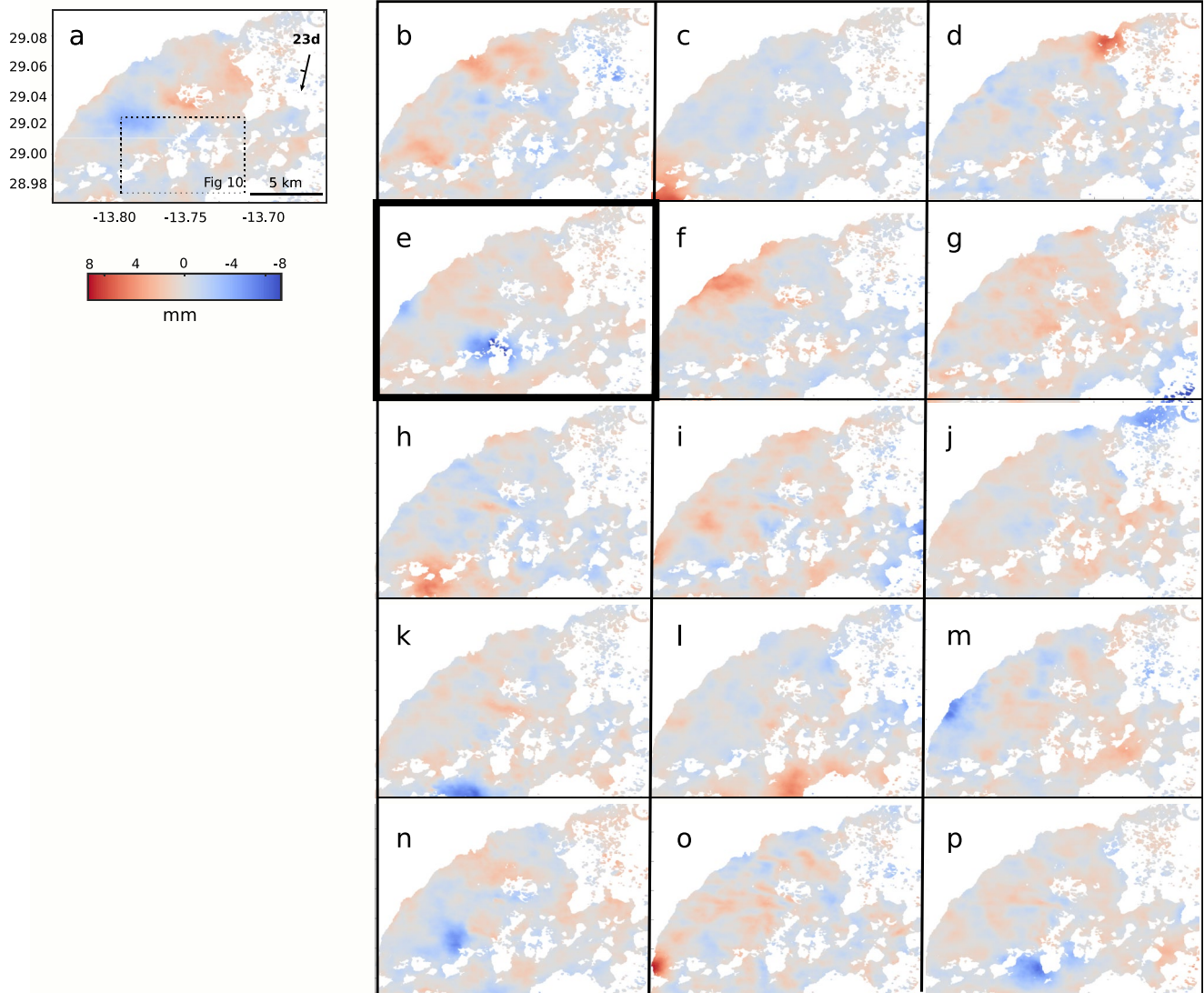
Figure A8. Representative independent spatial components from decomposition of 26 3-year descending stacks of data (track 023d). The component identified as Timanafaya lava flow displacements is indicated by the black box. This spatial pattern was retrieved with every independent restart of the FastICA algorithm. Other spatial components include both turbulent atmospheric patterns associated with single epochs, and patterns attributable to topographically correlated atmospheric features that appear in multiple interferograms. Please note that the sign and magnitudes shown here are arbitrary as they trade off with the corresponding mixing matrix values.
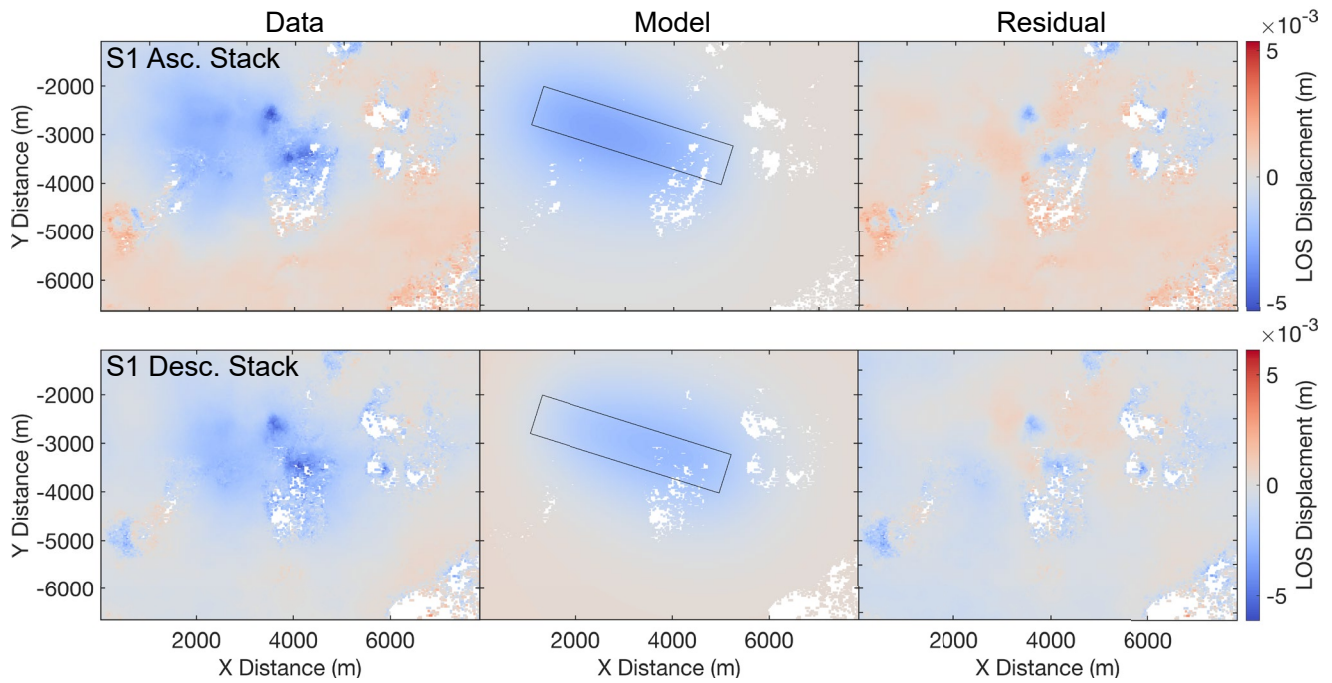
Figure A9. Best fit sill models and residuals using Geodectic Bayesian Inversion Software for the displacement at Timanfaya in the stacked Sentinel-1 data set. Note positions are relative to an arbitrary origin point −13.79°E, 29.03°N. The upper row shows the data, model, and residual for the ascending data set, while the lower row shows the same for the descending data set. This optimal spatial geometry is illustrated as a black rectangle, in the "Model" panel of each row.
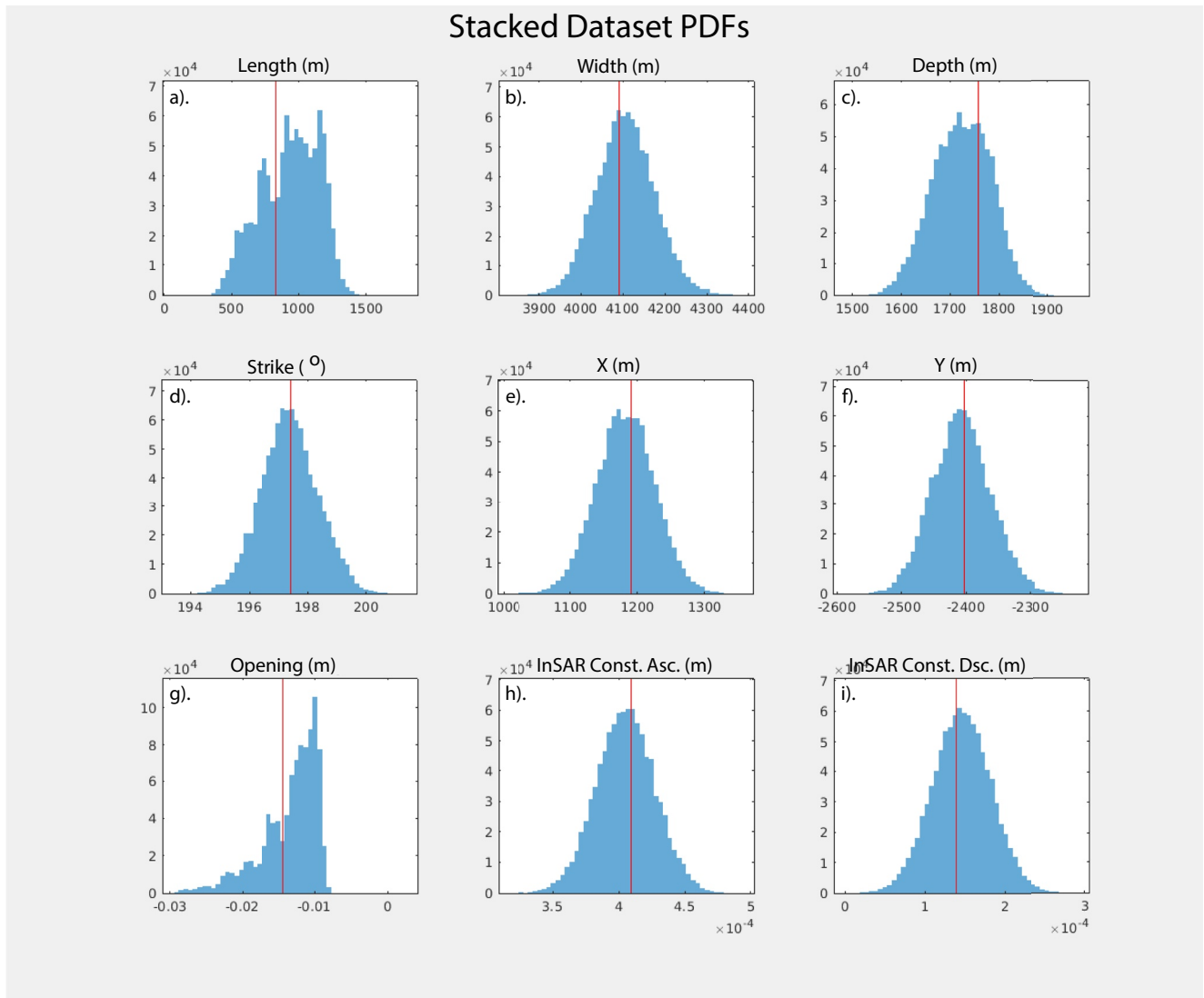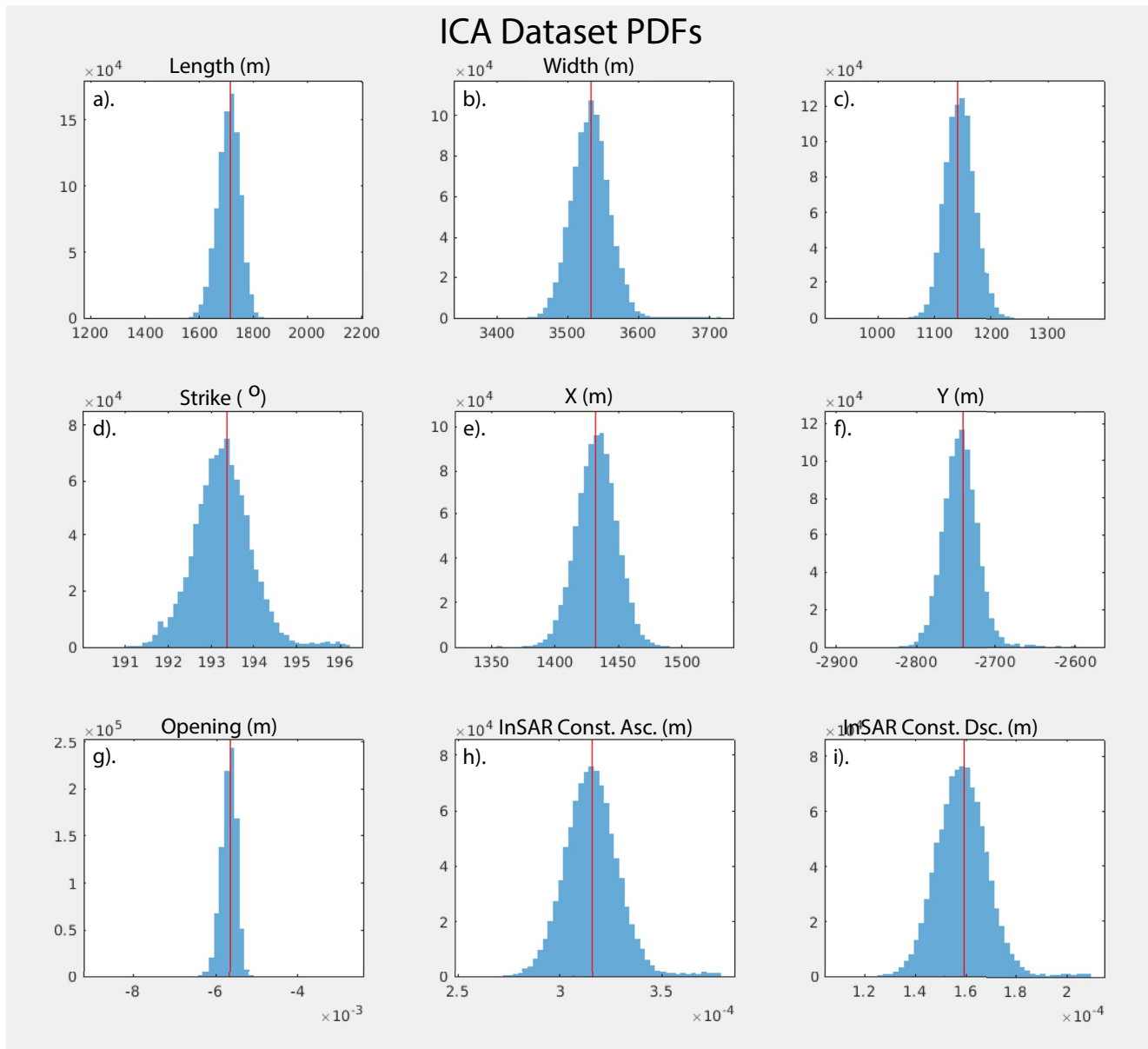
Figure A10. Histograms of posterior density functions for each source parameter for the stacked data set. In each case blue bars illustrate the histogram, while the red line shows the optimal value. (a) PDF of the length of horizontal edge of the sill in meters. (b) PDF of the width of horizontal edge of the sill in meters. (c) PDF of the depth of the sill in meters (positive downwards). (d) PDF of sill strike angle in degrees, relative to North. (e) PDF of X-coordinate of sill edge in meters, relative to a local reference point. (f) PDF of Y-coordinate of sill edge in meters, relative to a local reference point. (g). PDF of sill opening (change in thickness) in meters. (h, i). PDF of estimated line-of-sight Interferometric Synthetic Aperture Radar constant offset, in meters.

Figure A11. Histograms of posterior density functions for each source parameter for the independent component analysis data set. In each case blue bars illustrate the histogram, while the red line shows the optimal value. (a) PDF of the length of horizontal edge of the sill in meters. (b) PDF of the width of horizontal edge of the sill in meters. (c) PDF of the depth of the sill in meters (positive downwards). (d) PDF of sill strike angle in degrees, relative to North. (e) PDF of X-coordinate of sill edge in meters, relative to a local reference point. (f) PDF of Y-coordinate of sill edge in meters, relative to a local reference point. (g). PDF of sill opening (change in thickness) in meters. (h, i). PDF of estimated line-of-sight Interferometric Synthetic Aperture Radar constant offset, in meters.

Data Availability Statement

The ENVISAT and Sentinel-1 datasets prepared for analysis in this paper are made available through Zenodo (Purcell et al., 2022). Additionally, this paper contains Copernicus Sentinel data (2014–2020) and the original Sentinel-1 SAR SLC data are copyrighted by the European Space Agency (ESA) and are distributed through the Alaska Satellite Facility Distributed Active Archive Center (https://search.asf.alaska.edu/#/?zoom=9.798 &center=-14.000,28.991&polygon=POLYGON((-13.9704%2028.8027,-13.4596%2028.7934,-13.3827%20 29.2879,-13.9261%2029.2952,-13.9704%2028.8027))&start=2014-06-14T23:00:00Z&end=2020-07-31T22:59 :59Z&productTypes=SLC&beamModes=IW&resultsLoaded=true&granule=S1A_IW_SLC__1SDV_2020073

1T065425_20200731T065452_033695_03E7C4_6A67-SLC). The Sentinel-1 velocities were calculated using the open source package LiCSBAS, available at https://github.com/yumorishita/LiCSBAS. Atmospheric weather model corrections are available from the Generic Atmospheric Correction Online Service for InSAR (GACOS) available at http://www.gacos.net/. LiDAR point cloud DEM data are available from the Spanish National Geographic Information Center (CNIG): https://centrodedescargas.cnig.es/CentroDescargas/. GNSS data are openly available from the Nevada Geodetic Laboratory, University of Nevada, Reno (http://geodesy.unr.edu/NGLStationPages/stations/TIAS.sta; http://geodesy.unr.edu/NGLStationPages/stations/YAIZ.sta).

References

Anguita, F., & Hernán, F. (2000). The Canary Islands origin: A unifying model. *Journal of Volcanology and Geothermal Research*, *103*(1), 1–26. https://doi.org/10.1016/S0377-0273(00)00195-5

Annen, C. (2017). Factors affecting the thickness of thermal aureoles. *Frontiers of Earth Science*, *5*. https://doi.org/10.3389/feart.2017.00082

Ansari, H., De Zan, F., & Parizzi, A. (2021). Study of systematic bias in measuring surface deformation with SAR interferometry. *IEEE Transactions on Geoscience and Remote Sensing*, *59*(2), 1285–1301. https://doi.org/10.1109/TGRS.2020.3003421

Araña, V., Diez, J. L., Ortiz, R., & Yuguero, J. (1984). Convection of geothermal fluids in the timanfaya volcanic area (Lanzarote, Canary Islands). *Bulletin Volcanologique*, *47*(3), 667–677. https://doi.org/10.1007/BF01961234

Araña, V., Ortiz, R., & Yuguero, J. (1973). Thermal anomalies in lanzarote (Canary Islands). *Geothermics*, *2*(2), 73–75. https://doi.org/10.1016/0375-6505(73)90006-0

Bagnardi, M., & Hooper, A. (2018). Inversion of surface deformation data for rapid estimates of source parameters and uncertainties: A Bayesian approach. *Geochemistry, Geophysics, Geosystems*, *19*(7), 2194–2211. https://doi.org/10.1029/2018GC007585

Berardino, P., Fornaro, G., Lanari, R., & Sansosti, E. (2002). A new algorithm for surface deformation monitoring based on small baseline differential SAR interferograms. *IEEE Transactions on Geoscience and Remote Sensing*, *40*(11), 2375–2383. https://doi.org/10.1109/TGRS.2002.803792

Blanco-Montenegro, I., Montesinos, F. G., & Arnoso, J. (2018). Aeromagnetic anomalies reveal the link between magmatism and tectonics during the early formation of the Canary Islands. *Scientific Reports*, *8*(1), 42. https://doi.org/10.1038/s41598-017-18813-w

Blewitt, G., Hammond, W. C., & Kreemer, C. (2018). Harnessing the GPS data explosion for interdisciplinary science. *Eos*, *99*. https://doi.org/10.1029/2018EO104623

Button, A., & Cawthorn, R. G. (2015). Distribution of mafic sills in the transvaal supergroup, northeastern South Africa. *Journal of the Geological Society*, *172*(3), 357–367. https://doi.org/10.1144/jgs2014-101

Camacho, A. G., Montesinos, F. G., Vieira, R., & Arnoso, J. (2001). Modelling of crustal anomalies of Lanzarote (Canary Islands) in light of gravity data. *Geophysical Journal International*, *147*(2), 403–414. https://doi.org/10.1046/j.0956-540x.2001.01546.x

Camacho, A. G., Prieto, J. F., Ancochea, E., & Fernández, J. (2019). Deep volcanic morphology below Lanzarote, Canaries, from gravity inversion: New results for timanfaya and implications. *Journal of Volcanology and Geothermal Research*, *369*, 64–79. https://doi.org/10.1016/j.jvolgeores.2018.11.013

Cao, Y., Jónsson, S., & Li, Z. (2021). Advanced InSAR tropospheric corrections from global atmospheric models that incorporate spatial stochastic properties of the troposphere. *Journal of Geophysical Research: Solid Earth*, *126*(5), e2020JB020952. https://doi.org/10.1029/2020JB020952

Caricchi, L., Biggs, J., Annen, C., & Ebmeier, S. (2014). The influence of cooling, crystallisation and re-melting on the interpretation of geodetic signals in volcanic systems. *Earth and Planetary Science Letters*, *388*, 166–174. https://doi.org/10.1016/j.epsl.2013.12.002

Carracedo, J. C. (2014). The 1730–1736 eruption of Lanzarote, Canary Islands. In F. Gutiérrez & M. Gutiérrez (Eds.), *Landscapes and Landforms of Spain* (pp. 273–288). Springer Netherlands. https://doi.org/10.1007/978-94-017-8628-7_23

Carracedo, J. C., Day, S., Guillou, H., Badiola, E. R., Canas, J. A., & Torrado, F. J. P. (1998). Hotspot volcanism close to a passive continental margin: The Canary Islands. *Geological Magazine*, *135*(5), 591–604. https://doi.org/10.1017/S0016756898001447

Carracedo, J. C., Rodriguez Badiola, E., & Soler, V. (1992). The 1730–1736 eruption of Lanzarote, Canary Islands: A long, high-magnitude basaltic fissure eruption. *Journal of Volcanology and Geothermal Research*, *53*(1), 239–250. https://doi.org/10.1016/0377-0273(92)90084-Q

Carracedo, J. C., Troll, V. R., Day, J. M. D., Geiger, H., Junca, M. A., Soler, V., et al. (2022). The 2021 eruption of the Cumbre Vieja Volcanic Ridge on La Palma.

Chaussard, E. (2016). Subsidence in the Parícutin lava field: Causes and implications for interpretation of deformation fields at volcanoes. *Journal of Volcanology and Geothermal Research*, *320*, 1–11. https://doi.org/10.1016/j.jvolgeores.2016.04.009

Chen, C. W., & Zebker, H. A. (2000). Network approaches to two-dimensional phase unwrapping: Intractability and two new algorithms. *Journal of the Optical Society of America*, *17*(3), 401–414. https://doi.org/10.1364/JOSAA.17.000401

Comon, P. (1994). Independent component analysis, A new concept? *Signal Processing*, *36*(3), 287–314. https://doi.org/10.1016/0165-1684(94)90029-9

De Zan, F., & Gomba, G. (2018). Vegetation and soil moisture inversion from SAR closure phases: First experiments and results. *Remote Sensing of Environment*, *217*, 562–572. https://doi.org/10.1016/j.rse.2018.08.034

De Zan, F., Parizzi, A., Prats-Iraola, P., & López-Dekker, P. (2014). A SAR interferometric model for soil moisture. *IEEE Transactions on Geoscience and Remote Sensing*, *52*(1), 418–425. https://doi.org/10.1109/TGRS.2013.2241069

De Zan, F., Zonno, M., & López-Dekker, P. (2015). Phase inconsistencies and multiple scattering in SAR interferometry. *IEEE Transactions on Geoscience and Remote Sensing*, *53*(12), 6608–6616. https://doi.org/10.1109/TGRS.2015.2444431

Ebmeier, S. K. (2016). Application of independent component analysis to multitemporal InSAR data with volcanic case studies. *Journal of Geophysical Research: Solid Earth*, *121*(12), 8970–8986. https://doi.org/10.1002/2016JB013765

Ebmeier, S. K., Biggs, J., Mather, T. A., & Amelung, F. (2013). On the lack of InSAR observations of magmatic deformation at Central American volcanoes. *Journal of Geophysical Research: Solid Earth*, *118*(5), 2571–2585. https://doi.org/10.1002/jgrb.50195

Ebmeier, S. K., Biggs, J., Mather, T. A., Elliott, J. R., Wadge, G., & Amelung, F. (2012). Measuring large topographic change with InSAR: Lava thicknesses, extrusion rate and subsidence rate at Santiaguito volcano, Guatemala. *Earth and Planetary Science Letters*, *335–336*, 216–225. https://doi.org/10.1016/j.epsl.2012.04.027

Farr, T. G., Rosen, P. A., Caro, E., Crippen, R., Duren, R., Hensley, S., et al. (2007). The shuttle radar topography mission. *Reviews of Geophysics*, *45*(2), RG2004. https://doi.org/10.1029/2005RG000183

Gaddes, M. E., Hooper, A., & Bagnardi, M. (2019). Using machine learning to automatically detect volcanic unrest in a time series of interferograms. *Journal of Geophysical Research: Solid Earth*, *124*(11), 12304–12322. https://doi.org/10.1029/2019JB017519

Ghiorso, M. S., & Gualda, G. A. R. (2015). Chapter 6—Chemical thermodynamics and the study of magmas. In H. Sigurdsson (Ed.), *The encyclopedia of volcanoes* (2nd ed., pp. 143–161). Academic Press. https://doi.org/10.1016/B978-0-12-385938-9.00006-7

Goldstein, R. M., & Werner, C. L. (1998). Radar interferogram filtering for geophysical applications. *Geophysical Research Letters*, *25*(21), 4035–4038. https://doi.org/10.1029/1998GL900033

González, P. J. (2022). Volcano-tectonic control of Cumbre Vieja. *Science*, *375*(6587), 1348–1349. https://doi.org/10.1126/science.abn5148

González, P. J., & Fernández, J. (2011). Error estimation in multitemporal InSAR deformation time series, with application to Lanzarote, Canary Islands. *Journal of Geophysical Research*, *116*(B10), B10404. https://doi.org/10.1029/2011JB008412

González, P. J., Tiampo, K. F., Camacho, A. G., & Fernández, J. (2010). Shallow flank deformation at Cumbre Vieja volcano (Canary Islands): Implications on the stability of steep-sided volcano flanks at oceanic islands. *Earth and Planetary Science Letters*, *297*(3), 545–557. https://doi.org/10.1016/j.epsl.2010.07.006

Gualda, G. A. R., Ghiorso, M. S., Lemons, R. V., & Carley, T. L. (2012). Rhyolite-MELTS: A modified calibration of MELTS optimized for silica-rich, fluid-bearing magmatic systems. *Journal of Petrology*, *53*(5), 875–890. https://doi.org/10.1093/petrology/egr080

Gudmundsson, M. T., Larsen, G., Höskuldsson, Á., & Gylfason, Á. G. (2008). Volcanic hazards in Iceland. *Jökill*, *19*.

Hamlyn, J., Wright, T., Walters, R., Pagli, C., Sansosti, E., Casu, F., et al. (2018). What causes subsidence following the 2011 eruption at Nabro (Eritrea)? *Progress in Earth and Planetary Science*, *5*(1), 31. https://doi.org/10.1186/s40645-018-0186-5

Hoernle, K., & Schmincke, H.-U. (1993). The role of partial melting in the 15-Ma geochemical evolution of gran Canaria: A blob model for the Canary hotspot. *Journal of Petrology*, *34*(3), 599–626. https://doi.org/10.1093/petrology/34.3.599

Hyvärinen, A., & Oja, E. (1997). A fast fixed-point algorithm for independent component analysis. *Neural Computation*, *9*(7), 1483–1492. https://doi.org/10.1162/neco.1997.9.7.1483

Hyvärinen, A., & Oja, E. (2000). Independent component analysis: Algorithms and applications. *Neural Networks*, *13*(4), 411–430. https://doi.org/10.1016/S0893-6080(00)00026-5

IDECanarias visor 4.5.1. (n.d.). IDECanarias visor 4.5.1. Retrieved from https://visor.grafcan.es/visorweb/

Kampes, B., Hanssen, R. F., & Perski, Z. (2004). Radar interferometry with public domain tools. In *FRINGE 2003 workshop* (Vol. *550*).

Lazecký, M., Spaans, K., González, P. J., Maghsoudi, Y., Morishita, Y., Albino, F., et al. (2020). LiCSAR: An automatic InSAR tool for measuring and monitoring tectonic and volcanic activity. *Remote Sensing*, *12*(15), 2430. https://doi.org/10.3390/rs12152430

Li, Z., Cao, Y., Wei, J., Duan, M., Wu, L., Hou, J., & Zhu, J. (2019). Time-series InSAR ground deformation monitoring: Atmospheric delay modeling and estimating. *Earth-Science Reviews*, *192*, 258–284. https://doi.org/10.1016/j.earscirev.2019.03.008

Longpré, M.-A., & Felpeto, A. (2021). Historical volcanism in the Canary Islands; part 1: A review of precursory and eruptive activity, eruption parameter estimates, and implications for hazard assessment. *Journal of Volcanology and Geothermal Research*, *419*, 107363. https://doi.org/10.1016/j.jvolgeores.2021.107363

Maghsoudi, Y., Hooper, A. J., Wright, T. J., Lazecky, M., & Ansari, H. (2022). Characterizing and correcting phase biases in short-term, multilooked interferograms. *Remote Sensing of Environment*, *275*, 113022. https://doi.org/10.1016/j.rse.2022.113022

Maubant, L., Pathier, E., Daout, S., Radiguet, M., Doin, M.-P., Kazachkina, E., et al. (2020). Independent component analysis and parametric approach for source separation in InSAR time series at regional scale: Application to the 2017–2018 slow slip event in Guerrero (Mexico). *Journal of Geophysical Research: Solid Earth*, *125*(3), e2019JB018187. https://doi.org/10.1029/2019JB018187

Michaelides, R. J., Zebker, H. A., & Zheng, Y. (2019). An algorithm for estimating and correcting decorrelation phase from InSAR data using closure phase triplets. *IEEE Transactions on Geoscience and Remote Sensing*, *57*(12), 10390–10397. https://doi.org/10.1109/TGRS.2019.2934362

Morishita, Y. (2021). Nationwide urban ground deformation monitoring in Japan using Sentinel-1 LiCSAR products and LiCSBAS. *Progress in Earth and Planetary Science*, *8*(1), 6. https://doi.org/10.1186/s40645-020-00402-7

Morishita, Y., Lazecky, M., Wright, T. J., Weiss, J. R., Elliott, J. R., & Hooper, A. (2020). LiCSBAS: An open-source InSAR time series analysis package integrated with the LiCSAR Automated Sentinel-1 InSAR Processor. *Remote Sensing*, *12*(3), 424. https://doi.org/10.3390/rs12030424

Neal, C. A., Brantley, S. R., Antolik, L., Babb, J. L., Burgess, M., Calles, K., et al. (2019). The 2018 rift eruption and summit collapse of Kīlauea Volcano. *Science*, *363*(6425), 367–374. https://doi.org/10.1126/science.aav7046

Negredo, A. M., van Hunen, J., Rodríguez-González, J., & Fullea, J. (2022). On the origin of the Canary Islands: Insights from mantle convection modelling. *Earth and Planetary Science Letters*, *584*, 117506. https://doi.org/10.1016/j.epsl.2022.117506

Nikkhoo, M., Walter, T. R., Lundgren, P. R., & Prats-Iraola, P. (2017). Compound dislocation models (CDMs) for volcano deformation analyses. *Geophysical Journal International*, *208*(2), 877–894. https://doi.org/10.1093/gji/ggw427

Okada, Y. (1985). Surface deformation due to shear and tensile faults in a half-space. *Bulletin of the seismological society of America*, *75*(4), 1135–1154. https://doi.org/10.1785/BSSA0750041135

Ortiz, R., Araña, V., Astiz, M., & Garcia, A. (1986). Magnetotelluric study of the Teide (Tenerife) and Timanfaya (Tanzarote) volcanic areas. *Journal of Volcanology and Geothermal Research*, *30*(3), 357–377. https://doi.org/10.1016/0377-0273(86)90061-2

Parker, A. L., Biggs, J., & Lu, Z. (2014). Investigating long-term subsidence at Medicine Lake Volcano, CA, using multitemporal InSAR. *Geophysical Journal International*, *199*(2), 844–859. https://doi.org/10.1093/gji/ggu304

Patrick, M. R., Dehn, J., & Dean, K. (2004). Numerical modeling of lava flow cooling applied to the 1997 Okmok eruption: Approach and analysis. *Journal of Geophysical Research*, *109*(B3), B03202. https://doi.org/10.1029/2003JB002537

Pausata, F. S. R., Chafik, L., Caballero, R., & Battisti, D. S. (2015). Impacts of high-latitude volcanic eruptions on ENSO and AMOC. *Proceedings of the National Academy of Sciences*, *112*(45), 13784–13788. https://doi.org/10.1073/pnas.1509153112

Pedersen, G. B. M., Höskuldsson, A., Dürig, T., Thordarson, T., Jónsdóttir, I., Riishuus, M. S., et al. (2017). Lava field evolution and emplacement dynamics of the 2014–2015 basaltic fissure eruption at Holuhraun, Iceland. *Journal of Volcanology and Geothermal Research*, *340*, 155–169. https://doi.org/10.1016/j.jvolgeores.2017.02.027

Peng, M., Lu, Z., Zhao, C., Motagh, M., Bai, L., Conway, B. D., & Chen, H. (2022). Mapping land subsidence and aquifer system properties of the Willcox Basin, Arizona, from InSAR observations and independent component analysis. *Remote Sensing of Environment*, *271*, 112894. https://doi.org/10.1016/j.rse.2022.112894

Purcell, V., Reddin, E., Ebmeier, S., Gonzalez, P. J., Watson, A., Morishita, Y., & Elliott, J. (2022). Nearly three centuries of lava flow subsidence at1 Timanfaya, Lanzarote. Zenodo. https://doi.org/10.5281/zenodo.6620524

Riccardi, U., Arnoso, J., Benavent, M., Vélez, E., Tammaro, U., & Montesinos, F. G. (2018). Exploring deformation scenarios in Timanfaya volcanic area (Lanzarote, Canary Islands) from GNSS and ground based geodetic observations. *Journal of Volcanology and Geothermal Research*, *357*, 14–24. https://doi.org/10.1016/j.jvolgeores.2018.04.009

Romero, C., Sánchez, N., Vegas, J., & Galindo, I. (2019). Historic volcanic landforms diversity on Lanzarote. In E. Mateo, J. Martínez-Frías, & J. Vegas (Eds.), *Lanzarote and Chinijo Islands Geopark: From Earth to Space* (pp. 47–73). Springer International Publishing. https://doi.org/10.1007/978-3-030-13130-2_4

Rueda, J., Abella, R., Blanco, M. J., Díaz, E. A., Domínguez, J., Domínguez, J., et al. (2020). *Revisión del catálogo sísmico de las Islas Canarias (1341-2000). Publicaciones de la Administración General del Estado*. Centro Nacional de Información Geográfica.

Schaefer, L. N., Lu, Z., & Oommen, T. (2016). Post-eruption deformation processes measured using ALOS-1 and UAVSAR InSAR at Pacaya Volcano, Guatemala. *Remote Sensing*, *8*(1), 73. https://doi.org/10.3390/rs8010073

Sharma, K. (2005). *The eruptions of Öraefajökull 1362 (Iceland) and Lanzarote 1730-36 (Canary Islands): Sulphur emissions and volcanology (Unpublished doctoral dissertation)*. The Open University.

Sigurardóttir, S. S., Gudmundsson, M. T., & Hreinsdóttir, S. (2015). Mapping of the Eldgjá lava flow on Mýrdalssandur with magnetic surveying. *Jökill*(65), 12.

Solana, M. C., Kilburn, C. R. J., Rodriguez Badiola, E., & Aparicio, A. (2004a). Fast emplacement of extensive pahoehoe flow-fields: The case of the 1736 flows from Montaña de las Nueces, Lanzarote. *Journal of Volcanology and Geothermal Research*, *132*(2), 189–207. https://doi.org/10.1016/S0377-0273(03)00345-7

Solana, M. C., Kilburn, C. R. J., Rodriguez Badiola, E., & Aparicio, A. (2004b). Fast emplacement of extensive pahoehoe flow-fields: The case of the 1736 flows from Montaña de las Nueces, Lanzarote. *Journal of Volcanology and Geothermal Research*, *132*(2), 189–207. https://doi.org/10.1016/S0377-0273(03)00345-7

Stevens, N. F., Wadge, G., Williams, C. A., Morley, J. G., Muller, J.-P., Murray, J. B., & Upton, M. (2001). Surface movements of emplaced lava flows measured by synthetic aperture radar interferometry. *Journal of Geophysical Research*, *106*(B6), 11293–11313. https://doi.org/10.1029/2000JB900425

Thorarinsson, S. (1969). The Lakagígar eruption of 1783. *Bulletin Volcanologique*, *33*(3), 910–929. https://doi.org/10.1007/BF02596756

Torres, R., Snoeij, P., Geudtner, D., Bibby, D., Davidson, M., Attema, E., et al. (2012). GMES Sentinel-1 mission. *Remote Sensing of Environment*, *120*, 9–24. https://doi.org/10.1016/j.rse.2011.05.028

van Wyk de Vries, B., & Matela, R. (1998). Styles of volcano-induced deformation: Numerical models of substratum flexure, spreading and extrusion. *Journal of Volcanology and Geothermal Research*, *81*(1), 1–18. https://doi.org/10.1016/S0377-0273(97)00076-0

Wadge, G., Zhu, M., Holley, R. J., James, I. N., Clark, P. A., Wang, C., & Woodage, M. J. (2010). Correction of atmospheric delay effects in radar interferometry using a nested mesoscale atmospheric model. *Journal of Applied Geophysics*, *72*(2), 141–149. https://doi.org/10.1016/j.jappgeo.2010.08.005

Webb, T. L., Wadge, G., & Pascal, K. (2020). Mapping water vapour variability over a mountainous tropical island using InSAR and an atmospheric model for geodetic observations. *Remote Sensing of Environment*, *237*, 111560. https://doi.org/10.1016/j.rse.2019.111560

Wegmüller, U., Werner, C., Strozzi, T., & Wiesmann, A. (2002). Phase unwrapping with GAMMA ISP technical report, 13-May-2002 (p. 12).

Werner, C., Wegmüller, U., Strozzi, T., & Wiesmann, A. (2000). Gamma SAR and interferometric processing software. In H. Sawaya-Lacoste (Ed.),, Ed., *Proceedings of ERS-ENVISAT Symposium, Gothenburg, Sweden, 15–20 October 2000* European Space Agency Publications Division.

Wiart, P., & Oppenheimer, C. (2000). Largest known historical eruption in Africa: Dubbi volcano, Eritrea, 1861. *Geology*, *28*(4), 291–294. https://doi.org/10.1130/0091-7613(2000)028<0291:lkheia>2.3.co;2

Wittmann, W., Sigmundsson, F., Dumont, S., & Lavallée, Y. (2017). Post-emplacement cooling and contraction of lava flows: InSAR observations and a thermal model for lava fields at Hekla volcano, Iceland. *Journal of Geophysical Research: Solid Earth*, *122*(2), 946–965. https://doi.org/10.1002/2016JB013444

Wright, T. J., Ebinger, C., Biggs, J., Ayele, A., Yirgu, G., Keir, D., & Stork, A. (2006). Magma-maintained rift segmentation at continental rupture in the 2005 Afar dyking episode. *Nature*, *442*(7100), 291–294. https://doi.org/10.1038/nature04978

Yagüe-Martínez, N., Prats-Iraola, P., Rodríguez González, F., Brcic, R., Shau, R., Geudtner, D., et al. (2016). Interferometric processing of Sentinel-1 TOPS data. *IEEE Transactions on Geoscience and Remote Sensing*, *54*(4), 2220–2234. https://doi.org/10.1109/TGRS.2015.2497902

Yang, W., Vecchi, G. A., Fueglistaler, S., Horowitz, L. W., Luet, D. J., Muñoz, Á. G., et al. (2019). Climate impacts from large volcanic eruptions in a high-resolution climate model: The importance of forcing structure. *Geophysical Research Letters*, *46*(13), 7690–7699. https://doi.org/10.1029/2019GL082367

Yu, C., Li, Z., & Penna, N. T. (2018). Interferometric synthetic aperture radar atmospheric correction using a GPS-based iterative tropospheric decomposition model. *Remote Sensing of Environment*, *204*, 109–121. https://doi.org/10.1016/j.rse.2017.10.038

Yu, C., Li, Z., Penna, N. T., & Crippa, P. (2018). Generic atmospheric correction model for interferometric synthetic aperture radar observations. *Journal of Geophysical Research: Solid Earth*, *123*(10), 9202–9222. https://doi.org/10.1029/2017JB015305

Yu, X., Hu, J., & Sun, Q. (2017). Estimating actual 2D ground deformations induced by underground activities with cross-heading InSAR measurements. *Journal of Sensors*, *2017*, e3170506. https://doi.org/10.1155/2017/3170506